ACS OMEGA

Article

Cite This: ACS Omega 2019, 4, 421−436

http://pubs.acs.org/journal/acsodf

Scalable Synthesis of Collagenic-Waste and Natural Rubber-Based Biocomposite for Removal of Hg(II) and Dyes: Approach for Cost-Friendly Waste Management

Nayan Ranjan Singha,*[,†] Chandan Roy,[†,‡] Manas Mahapatra,[†] Arnab Dutta,[†] Joy Sankar Deb Roy,[†] Madhushree Mitra,[‡] and Pijush Kanti Chattopadhyay*[,‡]

[†]Advanced Polymer Laboratory, Department of Polymer Science and Technology, and [‡]Department of Leather Technology, Government College of Engineering and Leather Technology (Post Graduate), Maulana Abul Kalam Azad University of Technology, Salt Lake, Kolkata 700106, West Bengal, India

Supporting Information

ABSTRACT: For initiating a prosperous cost-friendly waste management of small-scale industries, cow buffing dust (CBD), one of the abundantly available semisynthetic collagenic solid wastes, has been used as a nonsulfur cross-linker of natural rubber (NR) for fabricating an NRCBD−biocomposite superadsorbent. The as-prepared reusable biocomposite bearing variegated collagenic and noncollagenic N-donors, along with the O-donors, has been reported for ligand-selective preferential superadsorption from waste water. Thus, a CBD and NR-based scalable biocomposite bearing optimum cross-linking, excellent physicochemical properties, and reusability has been developed via systematic optimization of the torque and reaction time for cost-friendly adsorptive exclusion of dyes, such as 2,8-dimethyl-3,7-diamino-phenazine (i.e., safranine, SF) and (7-amino-8-phenoxazin-3-ylidene)-diethylazanium dichlorozinc dichloride (i.e., brilliant cresyl blue), BCB, and Hg(II). The CBD-aided curing of NR has been achieved through the formation of a cross-linked chromane-ring originated via reaction between the methylol-phenol ring of phenol-formaldehyde resin and isoprene unit of NR. The partial disappearance of unsaturation in cured-NRCBD, relative variation of crystallinity, surface properties, elevated thermal stabilities, and ligand-selective superadsorption have been studied by advanced microstructural analyses of unadsorbed and/or adsorbed NRCBD using Fourier transform infrared (FTIR), ^{13}C nuclear magnetic resonance, ultraviolet−visible, and O 1s-/N 1s-/C 1s-/Hg $4f_{7/2,5/2}$-X-ray photoelectron spectroscopies, thermogravimetric analysis, differential scanning calorimetry, X-ray diffraction, field emission scanning electron microscopy, energy-dispersive spectroscopy, and pH_{PZC}. Response surface methodology-based optimization has been employed to attain the optimum potential of NRCBD, considering the interactive effects between pH_i, temperature, and concentration of the dye. H-aggregate and time-dependent hypochromic effect has been observed during individual adsorption of dyes. Moreover, the prevalence of chemisorption via ionic interaction between NRCBD and SF, BCB, and Hg(II) has been realized by FTIR, fitting of kinetics data to the pseudosecond-order model, and measurement of activation energies. The Brunauer−Emmett−Teller and Langmuir isotherms fit the best to BCB and SF/Hg(II), respectively. Thermodynamically spontaneous chemisorption have shown the maximum adsorption capacities of 303.61, 46.14, and 166.46 mg g^{-1} for SF, BCB, and Hg(II), respectively, at low initial concentration of Hg(II)/dyes = 40 ppm, 303 K, and adsorbent dose = 0.01 g.

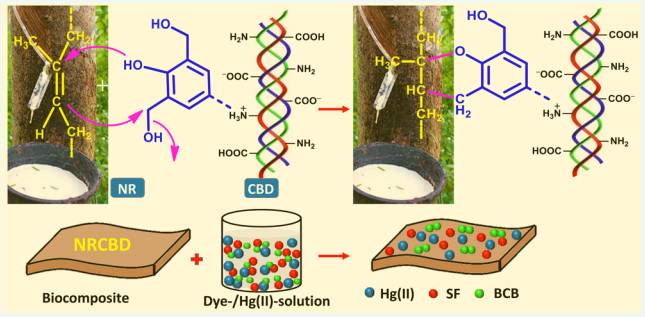

INTRODUCTION

Natural rubber (NR) exhibits excellent elasticity, flexibility, outstanding formability, biodegradability, resilience, and abrasion resistance. NR is one of the most important elastomers in terms of versatility and application volume. As uncured NR is sticky and inelastic, NR is cured to make more durable cross-linked material.[1,2] Theoretically, long chains of rubber molecules are cross-linked by vulcanization to convert a plastic-like soft material into a strong elastic product showing reversible deformability and good mechanical properties because of strain-induced crystallization, low hysteresis, excellent dynamic properties, and fatigue resistance. In addition to the traditional sulfur-vulcanization, there are several nonsulfur vulcanizing processes, which effectively produce diversified value-added products.[3,4]

Leather production is associated with the generation of a large quantity of collagenic wastes, such as cow buffing dust (CBD), fleshings, chrome shavings, and skin trimmings, of which CBD is

Received: October 14, 2018
Accepted: December 10, 2018
Published: January 7, 2019

DOI: 10.1021/acsomega.8b02799
ACS Omega 2019, 4, 421−436

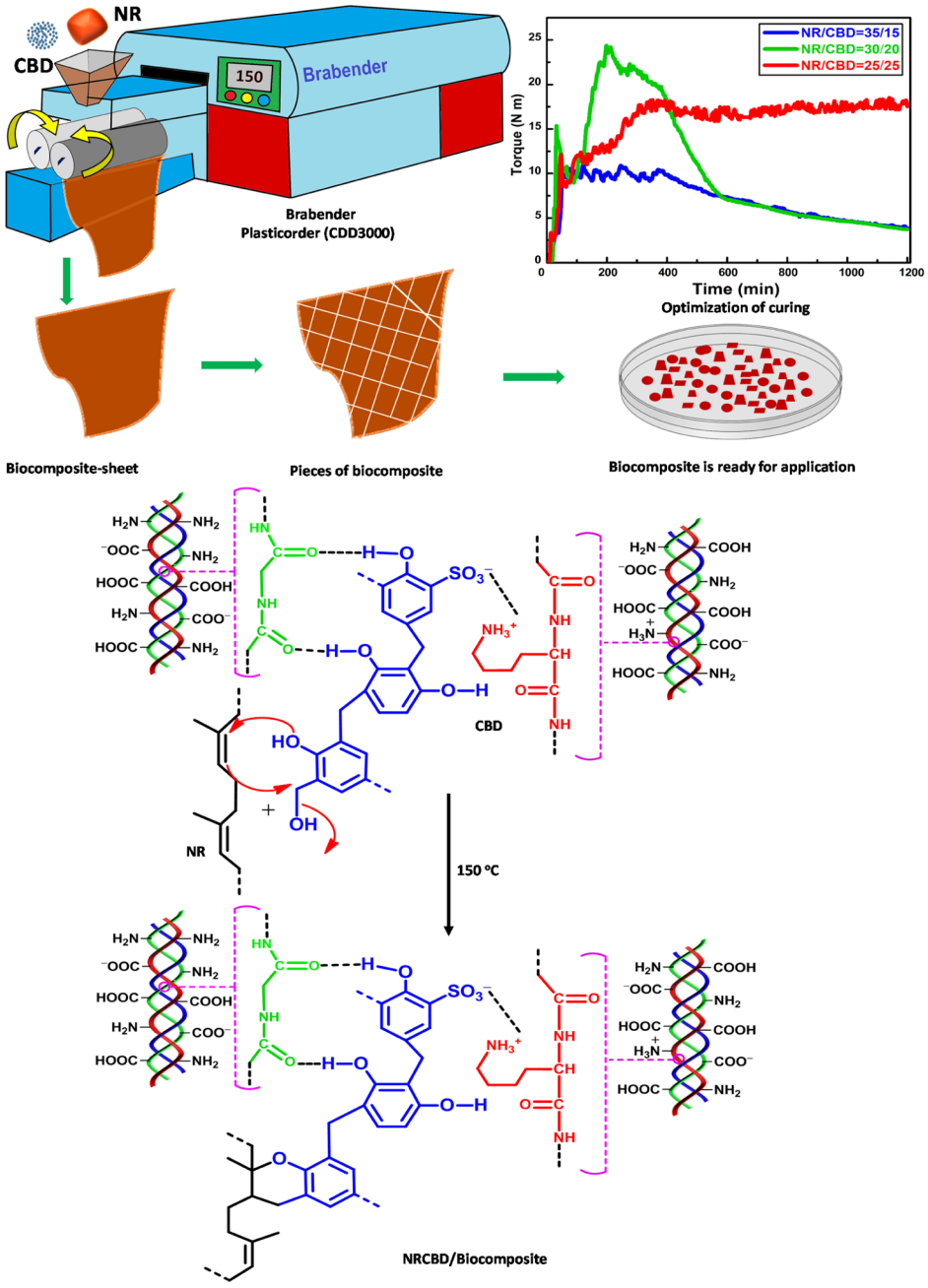

Figure 1. Synthesis of NRCBD−biocomposite adsorbent showing optimum physicochemical properties.

generated during the finishing operation. About, 2−6 kg CBD is generated as the solid waste per ton of skin/hide processed. CBD causes respiratory tract ailments, ulcers, perforated nasal septum, kidney malfunction, and lung cancer. For the safe disposal of CBD, though the starved air incineration is more acceptable than land disposal/thermal incineration, the technique is not viable because of the severe air pollution. Therefore, proper utilization of these hazardous wastes into valuable end products should be of paramount importance. Earlier, CBD was used to prepare activated charcoal of enhanced adsorption capacity (AC). Recently, CBD has been utilized as the reinforcing filler in carboxyl-terminated-,[5] carboxylated butadiene-acrylonitrile-, and butadiene-acrylonitrile-rubber[6] for substantial improvement of mechanical properties of composites. Alongside, CBD has been used as a binder in leather boards bearing reasonably robust mechanical properties.[7] However, the use of CBD and CBD-based materials as a cross-linker of rubber and adsorbents of dyes and metal ions, respectively, has not been reported till date.

CBD comprises of collagen, oil, inorganic-/organic-tanning agent, dyes, and fats. Thus, CBD contains different tanning agents, such as chromium complexes, resoles, polyphenolic compounds of tannins, and urea-formaldehyde, melamine-formaldehyde, and naphthalene-formaldehyde sulfonic acid condensates. Of these, resoles and bisphenol-based phenol-formaldehyde condensates are regularly used as synthetic tanning agents in leather, and thus, CBD contains significant amounts of such molecules. Except chromium complexes, most of the tanning agents, including bisphenol-based phenol-formaldehyde condensates, reversibly bind with collagen via H-bond and van der Waals interaction. Therefore, these reversibly bound tanning agents can be reutilized in preparing

DOI: 10.1021/acsomega.8b02799
ACS Omega 2019, 4, 421−436

Table 1. Characterization of NRCBD and Hg(II)/Dye-NRCBD

characterization technique	model/make	operational conditions
FTIR	spectrum-2, Singapore	performed using KBr pellet within 4000−400 cm^{-1}
^{13}C NMR	JEOL ECX400	performed at a frequency of 100 MHz
XPS	ESCA+, Omicron Nanotechnology, Oxford Instruments, Germany	performed at Al source (Kα radiation $h\nu$ = 1486.7 eV) monochromator at 15 kV and 20 mA
TGA	Pyris6 TGA, The Netherlands	operated in N_2 atmosphere with flow and scanning rates of 20.0 cm^3 min^{-1} and 10 °C min^{-1}, respectively, within 30−800 °C
DSC	Pyris6 DSC, The Netherlands	operated in N_2 atmosphere with flow rate of 20.0 cm^3 min^{-1} within 30−445 °C
XRD	X'Pert PRO, made by PANalytical B.V., The Netherlands using Ni-filtered Cu Kα radiation (λ = 1.5418 Å)	operated at the scanning rate of $2\theta = 0.005°$ s^{-1} and angle of diffraction from 2° to 72°
FESEM and EDX	JEOL JSM-7600F having resolution of 1 nm at 15 kV & 1.5 nm at 1 kV with the scanning voltage of 100 V to 30 kV	2.9 kV and 30k× magnification

some value-added products, such as biocomposite superadsorbents for the removal of water contaminants. Thus, bisphenol-based phenol-formaldehyde condensates function as nonsulfur vulcanizing agent of NR, in which the vulcanization mechanism preferably should follow the chromane mechanism instead of the allyl hydrogen mechanism. Moreover, other type of reactions, including Michelle's addition, may also occur in between unsaturation of NR and the primary amine of lysine side chain in CBD.

Chemical industries, such as textile, cosmetics, leather, plastic, paper, pharmaceutical, and food, use more than 10 000 types of synthetic dyes and pigments.[8] However, a large amount of such aromatic dyes is released as waste effluents causing serious pollution because of their carcinogenicity, teratogenicity, and mutagenicity. Safranine (SF) is regularly used as a colorant of natural fibers, such as wool, silk, and leather. Intrusion of SF in the human body produces several harmful effects including carcinogenicity, mitochondrial toxicity, and mutagenicity. Brilliant cresyl blue (BCB) is used to determine oxalate, formaldehyde, nitrite, protein, hydrazine, and cyclodextrin, and thus, a large amount of BCB is discharged to the environment. Alongside, BCB acts as photocatalyst, photoconductor, and fluorophore. BCB damages DNA through electrostatic attraction and/or intercalation. According to the United States Environmental Protection Agency, the maximum allowable limit of Hg(II) are 0.002 mg L^{-1} and 10 μg L^{-1} in drinking and waste water, respectively. Thus, it is essential to eliminate even trace amount of Hg(II) before discharging effluents into the environment for human safety and environmental protection.[9,10] All forms of mercury cause gastrointestinal disorder, neurologic malfunction, renal problem, and impose detrimental effects on lungs, kidneys, digestive system, brain, nervous system, endocrine system, and reproductive system in human-being.[11,12] Several methods, such as chemical oxidation, ion-exchange, biological treatment, photocatalytic degradation, adsorption,[13−16] membrane based separation,[17−19] precipitation,[20] ion exchange,[21] electro-deposition,[22] complexation,[23] electrostatic attraction,[24] and reverse osmosis,[25] have been employed. Of these, adsorption is the widely accepted promising method for water treatment because of the ease of operation and maintenance, cost effectiveness, high efficiency, flexibility, rapidness, simplicity of design, and availability of diversified adsorbents.[26] Alongside, response surface methodology (RSM) is employed for the evaluation of relative significance of several parameters in presence of complex interactions for attaining the maximum AC.[27−29]

In this work, attempts have been made to explore the vulcanizing potential of CBD in preparing NRCBD adsorbents. Moreover, the associated vulcanizing mechanism in the preparation of NRCBD-based adsorbents are to be explored, and thereby the dual performance of CBD, both as filler and vulcanizing agent, are to be investigated for efficient removal of Hg(II), SF, and BCB from waste water.

EXPERIMENTAL SECTION

Materials. $NaHCO_3$, $Na_2B_4O_7{\cdot}10H_2O$, KCl, CH_3COOH, CH_3COONa, HCl, and NaOH of analytical grades were purchased from Merck. NR of grade ribbed smoked sheets 3 (RSS3) and CBD were collected from PCBL (West Bengal, India) and local tannery (Bantala, Kolkata, West Bengal, India), respectively. BCB, SF, and chloride salt of Hg(II) were purchased from Sigma-Aldrich.

Synthesis of Stable Biocomposite-Adsorbent. In order to fabricate NRCBD, NR was selected as the matrix for carrying CBD via chemical bond formation. Three CBD cross-linked NR-based biocomposite adsorbents were fabricated by initial mastication of NR at 150 °C for 1 min in a two-shaft internal roller mixer bearing 70 mL capacity, wherein the mixing head was attached to a Brabender Plasticorder (CDD3000, Germany), followed by the rapid addition of 25, 20, and 15 g CBD to 25, 30, and 35 g NR, respectively, in the next minute. In this regard, as the mixing head is volume-sensitive, the loaded amount (i.e., 50 g) was restricted to 75% of mixer capacity. Thereafter, the mixing process was continued in the internal mixer at 150 °C for another 18 min at 60 rpm. The recorded plastographs showing variation of torque with time envisaged the curing characteristics encompassing the physical changes because of heating and chemical cross-linking. It was observed that all the plastographs consisted of several zones. Initially, a sharp increase in torque was observed for all biocomposites within the first 30 s because of the high viscosity of the inserted cold material (Figure 1). Thereafter, in the next 1 min, a zone of decreasing torque was manifested in all biocomposites because of material softening on heating till the attainment of the minimum torque. Subsequently, except NR/CBD = 35/15, commencement of another zone was observed, wherein rapid increase in torque was noted, and this particular zone was ascribed to the onset and progress of cross-linking. Notably, an insufficient amount of cross-links were formed in NR/CBD = 35/15 because of the relatively lower extent of CBD. Accordingly, massive cross-linking were originated in both NR/CBD = 30/20 and NR/CBD = 25/25.

Though the maximum torque attained by NR/CBD = 30/20 was significantly higher as compared to NR/CBD = 25/25, such an enhanced torque level was gradually deteriorated, which indicated the relatively unstable, that is, reversible nature of the

DOI: 10.1021/acsomega.8b02799
ACS Omega 2019, 4, 421−436

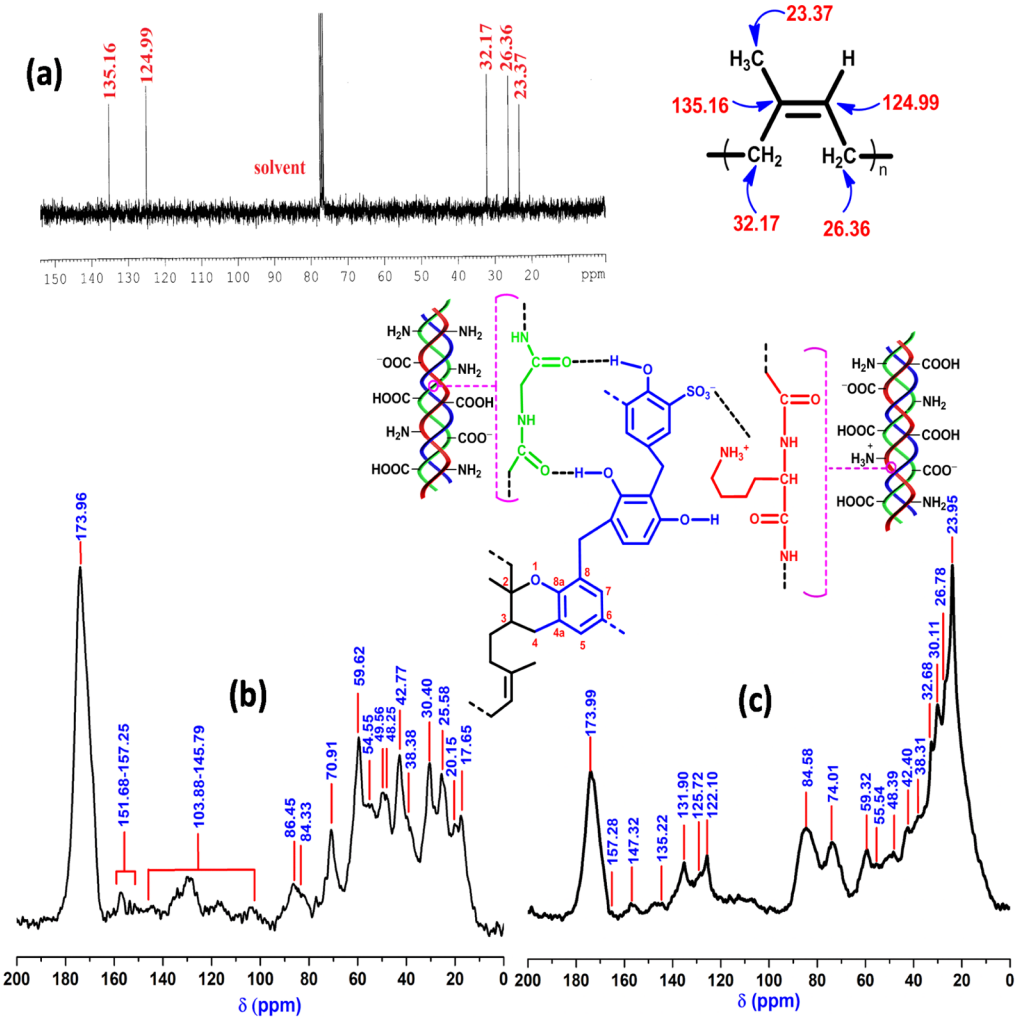

Figure 2. ^{13}C NMR of (a) NR, (b) CBD, and (c) NRCBD.

cross-links, and thus, the NR/CBD = 30/20 demonstrated reversion because of the cleavage of cross-links. In contrast, a significantly enhanced torque was maintained consistently in NR/CBD = 25/25, suggesting the formation of stable irreversible cross-links. Therefore, NRCBD bearing NR/CBD = 25/25 was selected as the most suitable and organized biocomposite-adsorbent.

Characterization. Unadsorbed and/or adsorbed NRCBD(s) were characterized by the techniques as given in Table 1. Alongside, NRCBD was characterized by pH_{PZC}. RSM, all graphic-based analyses, and drawing of chemical structures were carried out using Design-Expert 7.0.0, Origin 9.0 software, and ChemDraw Ultra 12.0 software, respectively.

Methodology. Solutions of $HgCl_2$, SF, and BCB were prepared by dissolving 5000 and 100 mg of $HgCl_2$ and SF/BCB, respectively, into 1000 mL distilled water. Solutions within 5−40 ppm were prepared by exact dilution of the stock solutions. 0.01 g dry NRCBDs were added to buffer solutions containing 25 mL Hg(II), SF, and BCB for individual adsorption. Thereafter, 25 mL buffer solution of pH_i = 7.0, 9.0, and 10.0 were added to Hg(II), SF, and BCB, respectively, at 300 rpm. After predetermined time intervals, the magnetic stirrer was stopped and the solution was allowed to settle for a couple of min. The progress of adsorption was monitored by withdrawing the supernatant solution, followed by measuring absorbance (A_t) at the respective λ_{max} to determine the residual concentration (C_t, mg L^{-1}) of Hg(II) and dyes using atomic absorption spectrometer (PerkinElmer AANALYST 100) and UV−vis spectrophotometer (PerkinElmer Lambda 365), respectively. From the precalibrated equation, the Hg(II)/dye concentration (C_t) was calculated, from which AC (i.e., AC/q_t, mg g^{-1}) was determined using eq 1.

$$q_t = \frac{(C_0 - C_t)V}{m_s} \quad (1)$$

Here, C_0/C_t (ppm), V (mL), and m_s (g) are feed Hg(II)/dye concentrations at $t = 0/t$, volume of adsorbate solution, and mass of NRCBD, respectively. After the attainment of equilibrium, the residual concentration (C_e, mg L^{-1}) was correlated with the equilibrium AC (q_e, mg g^{-1}) using eq 1.

RESULTS AND DISCUSSION

^{13}C NMR Analyses. The ^{13}C NMR spectrum of NR constituted of sp^3-C-specific peaks at 23.37, 26.36, and 32.17 ppm, which were attributed to −C(CH_3)=CH−, −C(CH_3)=CH−CH_2−, and −CH_2−C(CH_3)=CH−, respectively (Figure 2a). In addition, peaks at 124.99 and 135.16 ppm because of −C(CH_3)=CH− and −C(CH_3)=CH−, respectively, confirmed the presence of unsaturation (i.e., sp^2-C) in NR. CBD is composed of collagenic and noncollagenic processing materials,

DOI: 10.1021/acsomega.8b02799
ACS Omega 2019, 4, 421−436

such as methylol urea (MU), 1,1-/1,3-dimethylol urea (DMU), and trimethylol urea (TMU) of urea-formaldehyde resin and triazine of the melamine-formaldehyde resin. In this context, characteristic peaks at 173.96 and 70.91 ppm were attributed to >**C**=O of Gly/Pro/Hyp[30] and $\mathbf{C}_\gamma$ of Hyp/−NH**C**H_2OH of 1,1-DMU/−NH(**C**H_2OH)$_2$ of TMU/methylene diureas,[31] respectively, whereas peaks within 151.68−157.25 ppm were ascribed to $\mathbf{C}_\varepsilon$ of Arg[32]/>**C**=O of MU/1,3-DMU/1,1-DMU (Figure 2b).[31] Moreover, CBD-specific peaks at 59.62, 54.55, 49.56, 48.25, 30.40, 25.58, 20.15, and 17.65 ppm were attributed to $\mathbf{C}_\alpha$ of Pro/$\mathbf{C}_\alpha$ of Hyp, $\mathbf{C}_\delta$ of Hyp/$\mathbf{C}_\alpha$ of Glu/$\mathbf{C}_\alpha$ of Asp/$\mathbf{C}_\alpha$ of Lys, $\mathbf{C}_\alpha$ of Ala, $\mathbf{C}_\delta$ of Pro, $\mathbf{C}_\delta$ of Lys/$\mathbf{C}_\beta$ of Glu, $\mathbf{C}_\gamma$ of Lys, $\mathbf{C}_\gamma$ of Pro, and $\mathbf{C}_\beta$ of Ala, respectively.[30,32] The aromatic ring carbons of resol and *o*-cresol-/*p*-cresol-/phenol-/resorcinol-Novolac resins appeared within 103.88−145.79 ppm.

In NRCBD, although all the characteristic peaks of NR showed marginal shifts, relative intensities altered substantially (Table S1). As compared to NR, relative enhancement of intensities for both the olefinic carbons and notable increase in relative intensities for both −C(CH_3)=CH−**C**H_2− and −C(**C**H_3)=CH− confirmed substantial conversion of −C-(CH_3)=CH− into −CH(CH_3)−CH_2−. In this regard, CBD-aided change in intensities was ignored as CBD was devoid of peaks at 23.37, 26.36, 32.17, 124.99, and 135.16 ppm. In fact, sulfur-/nonsulfur-curing of NR usually accompanied by the substantial loss of unsaturation. NR-curing using CBD was confirmed from the arrival of CBD-specific peaks in NRCBD at 173.99, 157.28, 59.32, 55.54, 48.39, 30.11, 26.78, 20.17, and 17.62 ppm, attributed to >**C**=O of Gly/Pro/Hyp, $\mathbf{C}_\varepsilon$ of Arg[32]/>**C**=O of MU/1,3-DMU/1,1-DMU,[31] $\mathbf{C}_\alpha$ of Pro/$\mathbf{C}_\alpha$ of Hyp, $\mathbf{C}_\delta$ of Hyp/$\mathbf{C}_\alpha$ of Glu/$\mathbf{C}_\alpha$ of Asp/$\mathbf{C}_\alpha$ of Lys, $\mathbf{C}_\delta$ of Pro, $\mathbf{C}_\delta$ of Lys/$\mathbf{C}_\beta$ of Glu, $\mathbf{C}_\gamma$ of Lys, $\mathbf{C}_\gamma$ of Pro, and $\mathbf{C}_\beta$ of Ala, respectively.[31] In addition to the curing related loss of unsaturation, the formation of the chromane ring was inferred from the arrival of chromane ring-specific peaks at 32.68, 74.01, 122.10, and 147.32 because of **C**-3, **C**-2, **C**-4a, and **C**-8a, respectively, in NRCBD (Figure 2c).[33] Therefore, in NRCBD, the cross-linking of NR by tanning agents of CBD could be represented by the most widely accepted chromane mechanism related to resin curing of unsaturated rubber (Figure 1).

FTIR Analyses. In NRCBD, peaks at 1288, 984, and 2915 cm^{-1} appeared because of C=C−H in plane *bending*, C=C *twisting*, and C−H *sym. str.* of −CH_2−/−CH_3 adjacent to C=C of uncured-NR, respectively, receded from view because of the destruction of NR-specific C=C in NRCBD.[34] In this regard, the characteristic *sym. str.* Band-splitting of C−H into 2928 and 2915 cm^{-1}, observed usually in NR because of the double bond adjacent to −CH_3/−CH_2−, disappeared in NRCBD because of the reaction between C=C of NR and CBD (Figure 3). In fact, permanent disappearance of C=C of NR was realized from the obsolescence of peaks at 1288, 984, and 2915 cm^{-1} in all the Hg(II)-/dye-adsorbed NRCBD. Alongside, the massive loss of such unsaturation and thereby the formation of chromane rings was apprehended from NMR analyses (Figure 2). Indeed, alteration in NR-backbone via C=C led to obliteration of several NR-specific C−C vibrations at 490, 741, and 930/1009 cm^{-1} for C−C−C in plane *bending*, −CH_2− *rocking*, and C−C *str.*, respectively.[34] Alongside, as compared to CBD, the partial disappearance of −CH_2OH/O−H in NRCBD was realized from the obsolescence of the peak at 2876(sh), along with considerable decrease in the broad and intense peak from 3405 cm^{-1} of CBD to 3399 cm^{-1} in NRCBD (Figure 3). The formation of new type of ether linkages in NRCBD became

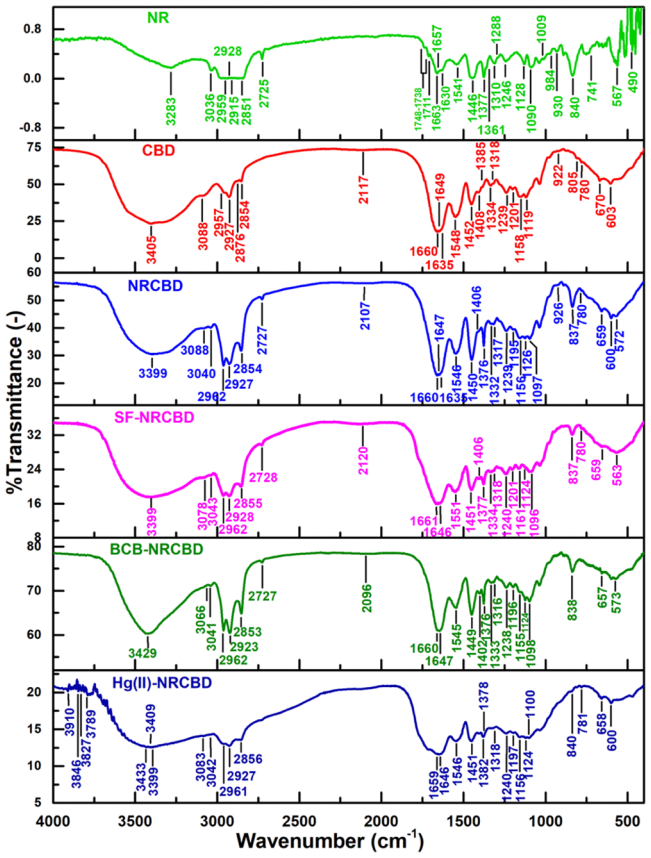

Figure 3. FTIR of NR, CBD, NRCBD, and SF-/BCB-/Hg(II)-NRCBD.

evident from substantial alteration of the spectrum within 1185−1085 cm^{-1}. In this regard, arrival of new peaks at 1126 and 1097 cm^{-1} were ascribed to C−O−C *sym. str.* and C−O−C *asym. str.* of alkyl−aryl ethers, respectively. Altogether, simultaneous destruction of NR-specific C=C, decrease in the number of −CH_2OH/O−H, and the formation of alkyl−aryl ether linkage could be commenced through the reaction between C=C of NR and −CH_2OH/O−H of the methylol-phenol ring of the phenol-formaldehyde resin in CBD for producing a new chromane ring in NRCBD.[35] Though chromane ring-specific peaks of CBD completely retained in NRCBD, the formation of new chromane rings or modification of existing chromanes were identified through varied shifts of characteristic chromane-based vibration frequencies from CBD to NRCBD (Table S2).[35]

Notably, the broad and intense peak of NRCBD at 3399 cm^{-1} became remarkably flattened and less intense in Hg(II)-NRCBD. In this regard, the arrival of new peaks at 3409 and 3433 cm^{-1} suggested appreciable destruction of preexisting N−H/O−H mutual H-bond of NRCBD in Hg(II)-NRCBD (Figure 3). The preferential association of Hg(II) with N-donor as compared to the O-donor ligand could be responsible for massive decrease in the N−H/O−H mutual H-bond, which led to the relatively higher population of O−H in Hg(II)-NRCBD. Such higher population of O−H was ascribed to the presence of Hg(OH)$_2$/H−Hg−OH/HgO in Hg(II)-NRCBD, realized from the arrival of several new peaks within 3910−3789 cm^{-1}. In addition, the preferable attachment of Hg(II) with the N-donor resulted in the complete omission of >NH^+−, >C=NH^+−, and >NH_2^+-specific peaks in Hg(II)-NRCBD.

DOI: 10.1021/acsomega.8b02799
ACS Omega 2019, 4, 421−436

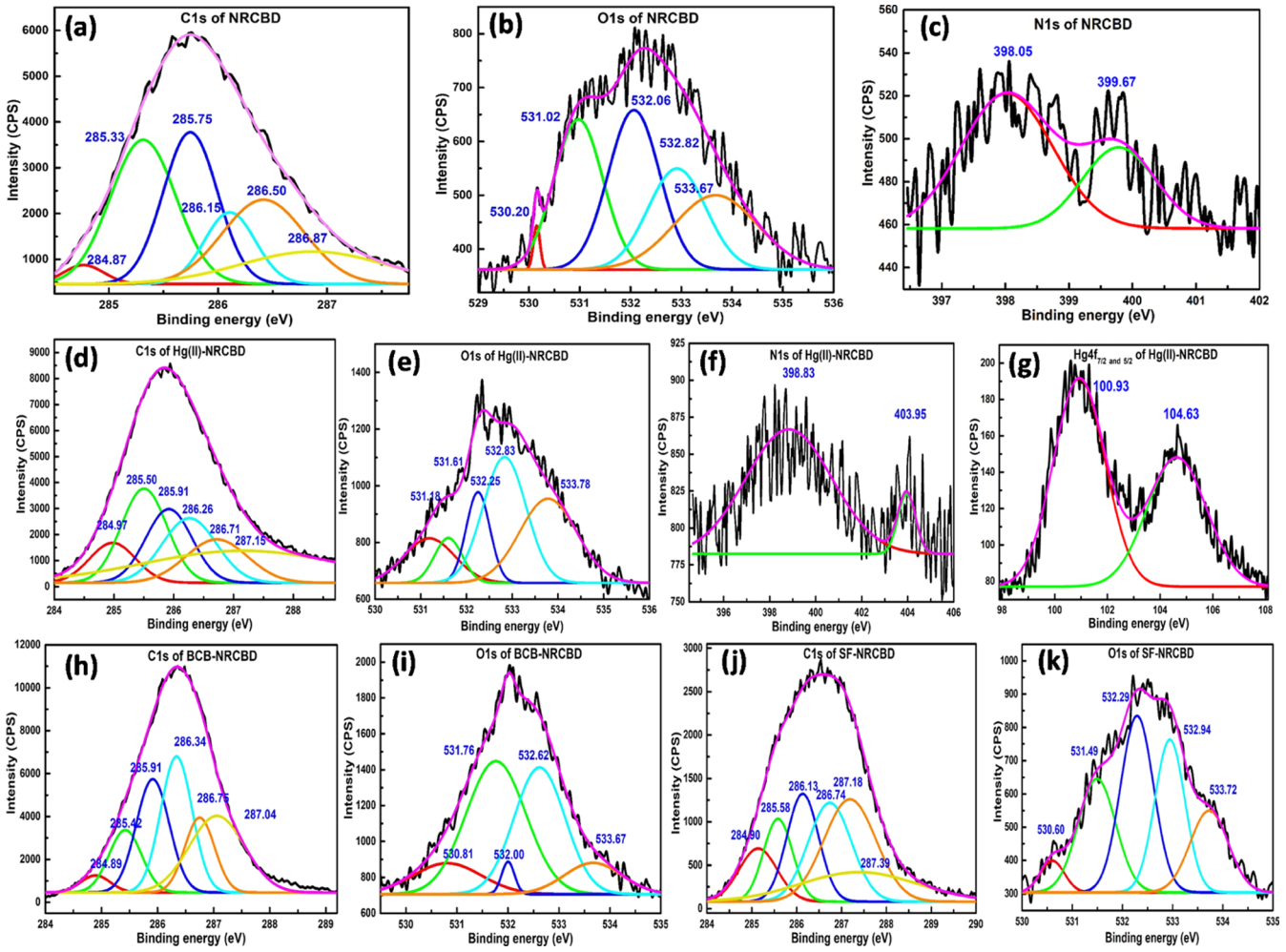

Figure 4. XPS analyses of C 1s (a,d,h,j) and O 1s (b,e,i,k) for NRCBD and Hg(II)-, BCB-, and SF-NRCBD, N 1s (c,f) for NRCBD and Hg(II)-NRCBD, and Hg $4f_{7/2}$ and $4f_{5/2}$ (g) for Hg(II)-NRCBD.

Interestingly, as a result of BCB adsorption, the N−H/O−H mutual H-bond peak shifted from 3399 of NRCBD to 3429 cm^{-1} in BCB-NRCBD, along with significant lowering of aromatic C−H *str*. form 3088 cm^{-1} of NRCBD to 3066 cm^{-1} in BCB-NRCBD (Figure 3). Additionally, in contrast to both NRCBD and SF-NRCBD, several peaks corresponding to strong O−H/O−H H-bond were found in BCB-NRCBD. All of these phenomena indicated the presence of BCB dimers or multilayers carrying sandwiched water entrapped via strong H-bond, as BCB tends to produce dimers at much lower concentration (i.e., 0.2×10^{-3} M). In contrast, all of these changes were not observed in SF-NRCBD, as SF is less prone to form dimers onto NRCBD during adsorption.[36] All other peaks of both SF-NRCBD and BCB-NRCBD retained, suggesting reversible interactions between dyes and NRCBD.

X-ray Photoelectron Spectroscopy Analyses. *NRCBD.* The deconvoluted C 1s spectrum of NRCBD constituted of peaks at 284.87, 285.33, 285.75, 286.15, 286.50, and 286.87 eV (Figure 4a) for C 1s of $-\mathbf{C}H_2-/-\mathbf{C}H_3$ of chromane/phenol, tertiary **C**−H, **C**1 of phenol, $\mathbf{C}_\alpha$ of amino acid, **C2** of chromane ring/ether, and >**C**═N of melamine/$-\mathbf{C}ONH_2$/−**C**ONH−/−**C**OOH, respectively. All of these peaks were significantly deviated from the usual NR peaks at 284.73, 285.00, and 285.28 eV for $-(CH_2\mathbf{C}H{=}\mathbf{C}(CH_3)CH_2)_n-$, $-(\mathbf{C}H_2CH{=}C(CH_3)\mathbf{C}H_2)_n-$, and $-(CH_2CH{=}C(\mathbf{C}H_3)CH_2)_n-$, respectively. Moreover, the O 1s peaks at 530.20, 531.02, 532.06, 532.82, and 533.67 eV (Figure 4b) were attributed to polysaccharides/glycosaminoglycans (GAGs), $Cr(\mathbf{O}H)_3$, >C═**O**, chromane/ether/$-CO\mathbf{O}^-$, and **O**−H, respectively. Alongside, the N 1s spectrum was deconvoluted into peaks at 398.05 and 399.67 eV (Figure 4c) designated to pyrrolidine units of proline/hydroxyproline and $-\mathbf{N}H-/-\mathbf{N}H_2$/C−**N** of collagen, respectively.[29] Accordingly, the prevalence of O 1s/N 1s-specific peaks in NRCBD confirmed the substantial incorporation of CBD into the NR-network. More importantly, as realized earlier from NMR and Fourier transform infrared (FTIR) results, the formation of the chromane ring or related ether linkages in NRCBD was substantiated from the newly generated C 1s peak at 286.50 eV in NRCBD that was attributed exclusively to the carbon attached to oxygen of the chromane ring or ether linkage produced via curing of NR by the Novolac component of CBD. Interestingly, almost similar kind of relative intensities of 0.211 and 0.205 for the chromane/ether/$-CO\mathbf{O}^-$-specific O 1s peak at 532.82 eV and chromane/ether-specific C 1s peak at 286.5 eV, respectively, confirmed the substantial prevalence of chromane rings in NRCBD. Simultaneously, the presence of $-CO\mathbf{O}^-$ was determined from the marginal difference between relative intensities (i.e., 0.211−0.205 = 0.05) of these peaks.

Hg(II)-NRCBD. Because of the binding between Hg(II) and NRCBD, the polysaccharides/GAGs and $Cr(\mathbf{O}H)_3$-specific O

DOI: 10.1021/acsomega.8b02799
ACS Omega 2019, 4, 421−436

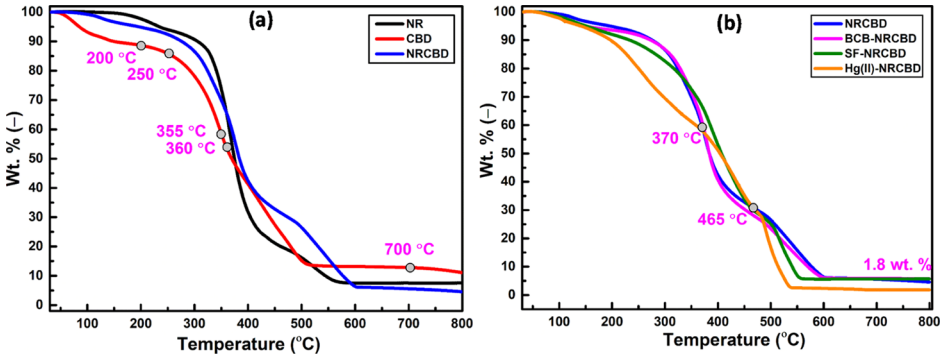

Figure 5. TGA of (a) NR, CBD, and NRCBD and (b) NRCBD, BCB-, SF-, and Hg(II)-NRCBD.

1s peaks of NRCBD were substantially raised to 531.18 and 531.61 eV (Figure 4e), respectively, indicating coordination of Hg(II) with O-donor of $-SO_3^-$ and chromium complexes, leading to the increased binding energies (BEs) and associated alterations in intensities of those O 1s peaks (Table S3). Moreover, the remaining O 1s peaks were marginally shifted from 532.06, 532.82, and 533.67 to 532.25, 532.83, and 533.78 eV in Hg(II)-NRCBD (Figure 4e), inferring ionization of −COOH and related weaker physicochemical interaction between O-donor and Hg(II). In this context, during Hg(II) adsorption, deprotonation of −COOH of NRCBD to $-COO^-$ at $pH_i > pH_{PZC}$ was ascertained from the appreciably elevated relative intensity of the O 1s peak from 0.211 at 532.82 eV of NRCBD to 0.342 at 532.83 eV in Hg(II)-NRCBD, along with reduced intensity of the >C═O peak from 0.294 at 532.06 eV of NRCBD to 0.135 at 532.25 eV in Hg(II)-NRCBD (Table S3). Surprisingly, despite ionization of −COOH to $-COO^-$, substantial increase in the intensity was noted for the O−H-specific peak from 0.22 at 533.67 eV to 0.30 at 533.78 eV, attributed to the deposition of $Hg(\mathbf{O}H)_2$ onto Hg(II)-NRCBD. Indeed, deposition of $Hg(\mathbf{O}H)_2$ and strong coordinate bonding between Hg(II) and N-donor of pyrrolidine of proline/hydroxyproline and $-\mathbf{N}H-/-\mathbf{N}H_2/C-\mathbf{N}$ of the collagen in NRCBD led to substantial changes in N 1s BEs to 398.83 and 403.95 eV in Hg(II)-NRCBD (Figure 4f), together with the decrease in $HgCl_2$-specific Hg $4f_{7/2}$- and Hg $4f_{5/2}$-BE from 102.58 and 106.68 to 100.93 and 104.63 eV in Hg(II)-NRCBD, respectively (Figure 4g).[37] Indeed, cumulative effects of Hg(II) adsorption and related phenomena were also reflected in both the altered C 1s peak positions (Figure 4d) and respective peak intensities in Hg(II)-NRCBD (Table S3).

BCB-NRCBD. The C 1s X-ray photoelectron spectroscopy (XPS) spectra of BCB-NRCBD comprised of peaks at 284.89, 285.42, 285.91, 286.34, 286.75, and 287.04 eV (Figure 4h), of which peaks at 284.89, 285.42, and 285.91 eV, assigned to $-\mathbf{C}H_2-/-\mathbf{C}H_3$ of chromane, tertiary **C**−H, and **C**1 of phenolic species, respectively, remained almost unaltered as compared to those of NRCBD, interpreting the least direct and/or indirect involvement of such group(s) in adsorption of BCB. However, peaks at 286.34, 286.75, and 287.04 eV because of $\mathbf{C}_\alpha$ of amino acid, **C**2 of chromane ring/ether, and >**C**═N of melamine/$-\mathbf{C}ONH_2/-\mathbf{C}ONH-/-\mathbf{C}OOH$, respectively, were shifted significantly toward higher BE than NRCBD. Such higher values of BEs could be explained by the decrease in electron densities at the C-donor via noncovalent interactions between the lone pair and/or negatively charged N−O adjacent to the C-donor and ammonium cation of BCB. Moreover, the appreciable increase in relative population of hydrophilic groups at the surface of BCB-NRCBD led to remarkable changes in the relative intensities of all C 1s peaks. Indeed, adsorption-driven relative lowering in the population of hydrophobic rubber moieties at the surface could be anticipated from the drastic drop in peak intensity corresponding to tertiary **C**−H and chromane-/ether-specific peaks at 285.42 and 286.75 eV. On contrary, increased population of hydrophilic parts at the surface, along with deposition of BCB increased the intensities of peaks. Alongside, BE of O 1s peaks were shifted to 530.81, 531.76, 532.00, 532.62, and 533.67 eV (Figure 4i), indicating the adsorption-driven alterations in physicochemical interactions of the adsorbed BCB-cation with the anionic part of NRCBD within BCB-NRCBD. Such ionic interactions and associated deprotonation of −COOH into $-COO^-$ were rationalized from the reasonable drop in intensity of C═**O** and **O**−H peaks at 532.00 and 533.67 eV, respectively, together with a significant gain in intensity of the $-COO^-$-specific peak. Besides, unprecedented rise in peak intensities at 530.81 and 531.76 eV was rationally understood from the significant deposition of Zn**O** and $Zn(\mathbf{O}H)_2$ onto BCB-NRCBD (Table S3). In this context, co-existence of $Zn(\mathbf{O}H)_2$ and Zn**O** at the BCB-NRCBD could be anticipated from the possible conversion of $ZnCl_4^{2-}$counter anion of BCB into $Zn(OH)_2$ at pH_i = 9.0, followed by transformation of $Zn(OH)_2$ into ZnO during drying of BCB-NRCBD at 70 °C.[38]

SF-NRCBD. Almost similar types of physicochemical interactions were confirmed in SF-NRCBD, wherein C 1s peaks were positioned at 284.90, 285.58, 286.13, 286.74, 287.18, and 287.39 eV (Figure 4j). Likewise, O 1s spectra of SF-NRCBD demonstrated significant alterations in peak positions with BEs of 530.60, 531.49, 532.29, 532.94, and 533.72 eV, indicating a substantial change in the electron cloud environment within SF-NRCBD (Figure 4k). For instance, similar to BCB-NRCBD, ionization of −COOH into $-COO^-$ could be understood from the drop of relative intensity at 533.72 eV, along with the increase in relative intensity at 532.94 eV.

Thermogravimetric Analysis Analyses. Within 30−200 °C, relatively higher weight loss of CBD (i.e., 11.4 wt %) as compared to NR (i.e., 2.4 wt %) (Figure 5a) was ascribed to the higher moisture content because of the prevalent hydrophilic constituents, such as tannin, synthetic tannin, protein, and fatty substances of CBD. Accordingly, relatively lower mass loss for NR was expected because of the strong hydrophobic nature of NR. Invariably, the extent of mass loss from NRCBD was in between NR and CBD. Notably, within 30−355 °C, the thermal stability was noted in the followed order: NR > NRCBD > CBD (Figure 5a). Such outcome was attributed to the relatively poor thermal stability of the collagen component in CBD, which underwent pronounced deamination from 250 to 360 °C,

DOI: 10.1021/acsomega.8b02799
ACS Omega 2019, 4, 421−436

resulting in the formation of ammonia via decomposition of −NH− and $-NH_2$ in arginine and lysine. In this context, arginine and lysine remain as 51 and 25 residues per 1000 residues of tropocollagen.[39] At the higher temperature range, that is, within 360−700 °C, relatively better thermal stability of NRCBD over NR/CBD was ascribed to the possible reaction between phenol-formaldehyde resin of CBD and isoprene units of NR, leading to the formation of new thermostable covalent linkage. The overall elevated thermal stability of NRCBD over NR was also substantiated by the appreciably higher DTG at 376 °C for NRCBD than the characteristic DTG of unvulcanized NR at 364 °C (Figure S1). Interestingly, beyond 360 °C, the thermal resistance of CBD exceeded appreciably as compared to NR.

It transpired that the prevalent thermo-resistant melamine-formaldehyde resin in CBD, confirmed from FTIR analysis, played a dominant role in enhancing the thermal stability of CBD as compared to NR. Notably, a drastic thermal degradation for Hg(II)-NRCBD was observed within 30−370 °C (Figure 5b). The lower boiling point of mercury and $HgCl_2$ was responsible for faster evaporation of loosely bound mercury components from Hg(II)-NRCBD.

However, within 370−465 °C, better thermal stability of Hg(II)-NRCBD than NRCBD was ascribed to the interaction between absorbed Hg(II) and nitrogen of the melamine to produce a thermo-resistant triazine ring-mercury assembly. However, beyond 465 °C, thermal stability of Hg(II)-NRCBD became inferior to that of NRCBD, attributed to the decomposition of triazine ring-mercury assembly and HgO in a rapid fashion. In this context, massive removal of mercury from Hg(II)-NRCBD was also reflected by the least residue (i.e., 1.8 wt %) (Figure 5b). Though the thermogravimetric analysis (TGA) plot of BCB-NRCBD was almost similar to that of NRCBD, the thermogram of SF-NRCBD was slightly different from both BCB-NRCBD and NRCBD. Such change was attributed to the greater adsorbing tendency of SF onto NRCBD, as SF shows relatively lesser dimer forming tendency than that of BCB and preferably remains as monomer in 0.2×10^{-3} M solution. On contrary, relatively higher dimer forming tendency of BCB was ascribed to the better relative affinity of BCB to remain mostly in the monomeric form at $<5 \times 10^{-5}$ M solution. Accordingly, penetration and diffusion of sterically favored SF-monomer into NRCBD was better than the BCB-dimer. In this context, the phenol-formaldehyde-based tanning reagent of CBD reacted with the C═C of NR to form chromanes (Figure 1).[40] However, according to the viewpoint of van der Meer, a methylene-quinone intermediate, generated from methylol-phenol of the phenol-formaldehyde resin, could also react at the methylene group adjacent to the C═C of the isoprene unit in NR (Scheme S1).[40]

Differential Scanning Calorimetry Analyses. The differential scanning calorimetry (DSC) thermogram of CBD demonstrated a broad and intense endothermic peak at 106 °C because of the moisture-enriched collagenic materials bearing variegated thermal stabilities as a result of diversified interactions between collagen and various tanning agents.[41] However, complete obsolescence of such a broad and intense peak in NRCBD was associated with substantial stabilization of the CBD-component in NRCBD via formation of the chromane ring. Indeed, owing to such curing-driven irreversible alterations, the CBD-specific peak at 106 °C never reappeared in Hg(II)-, BCB-, and SF-NRCBD (Figure S2). Alongside, CBD-aided curing of NR resulted in the elevated thermal resistance of NRCBD as compared to NR, realized from the complete disappearance of NR degradation-specific broad endothermic peak at 392 °C in NRCBD. Nevertheless, collagen degradation-related endothermic peaks were present both in CBD and NRCBD at 328 and 323 °C, respectively.[42] Moreover, endothermic transitions at 159/160, 164/163, and 394 °C because of the breakdown of methylol melamine, condensation reaction, and degradation of triazine rings of melamine formaldehyde, respectively,[43] were retained in the thermograms of both CBD and NRCBD, suggesting minimal interactions between the melamine formaldehyde components of CBD and NR in NRCBD (Figure S2). However, all of these melamine-specific endothermic peaks were disappeared in Hg(II)-NRCBD, suggesting stabilization of melamine components of CBD by Hg(II) via co-ordinate- or covalent-bonding, evidenced from XPS and TGA analyses.

X-ray Diffraction Analyses. The fibrous CBD showed intense peaks of collagen at 21.04° and 31.43° because of the amorphous scattering from randomly distributed components of collagen fibers and axial increase in distance (i.e., 2.80 Å) between the amino acid residues along collagen triple helices, respectively.[39,44] However, the relatively amorphous nature of NRCBD as compared to both NR and CBD indicated the complete destruction of the short range order in NRCBD because of the adequate intermingling of rubber and fibers in consequence to the reaction between rubber chains and phenol-formaldehyde-based component of CBD. Interestingly, the diffractogram of Hg(II)-NRCBD showed several sharp peaks of variable intensities (Figure S3). The sharp peak at 28.77° corresponding to 3.104 Å is almost identical to one of the dimensions of the HgO crystal (i.e., 3.111 Å), reflecting the FTIR results related to the deposition of HgO onto Hg(II)-NRCBD.[45] Besides, superficial deposition of mercuric chloride and mercuric amide chlorides was related to the use of mercuric chloride salt as adsorbate and stronger interaction of Hg(II) with the N-donor, as evidenced in the FTIR. As the adsorption was carried out at neutral pH, superficial depositions of mercuric hydroxide and mercuric oxide could strongly be recommended. Moreover, peaks at 44.40 and 46.84° were comparable to the 112 and 220 Miller planes of mercuric sulphate crystals deposited onto Hg(II)-NRCBD that altered sulfonic acid salt-related peaks in FTIR (Figure 3). Additionally, among the dye-adsorbed adsorbents, though SF-NRCBD was devoid of any peak, the diffractogram of BCB-NRCBD constituted of small peaks at 21.16, 43.53, 52.32, and 57.09°, which signified the mixed population of ε-$Zn(OH)_2$ and ZnO onto NRCBD.[38] Indeed, the presence of $Zn(OH)_2$ and ZnO onto BCB-NRCBD, inferred earlier in XPS analyses, was ascribed to the conversion of the $ZnCl_4^{2-}$-component of BCB into $Zn(OH)_2$ and ZnO because of the adsorption in the alkaline environment and subsequent dehydration of $Zn(OH)_2$ into ZnO at 70 °C.

SEM and Energy-Dispersive Spectroscopy Analyses. Fine structures of collagen fibers in CBD disappeared in the heterogeneous topography of NRCBD (Figure S4), suggesting the rubbery layer formation onto the collagen fibrils. The enormous phase mixing and complete destruction of the short range order in NRCBD was ascribed to the reaction between rubber chains and Novolac components of CBD, also evidenced from FTIR and X-ray diffraction (XRD) results. Moreover, postadsorptive particulate depositions onto Hg(II)-NRCBD were attributed to the presence of mercuric compounds because of the interaction between adsorbed Hg(II) and available functional groups of NRCBD (Figure S4).

DOI: 10.1021/acsomega.8b02799
ACS Omega 2019, 4, 421−436

Table 2. ANOVA Statistics of CCD for SF/BCB[a]

source	sum of squares	df	mean square	*F* value	*p*-value
Model	7001.94/6571.44	9/9	777.99/730.16	322.93/266.81	<0.0001*/<0.0001*
concentration of SF/BCB (mg L^{-1}, *A*)	3887.79/653.49	1/1	3887.79/653.49	1613.75/238.79	<0.0001*/<0.0001*
temperature (°C, *B*)	509.73/4.78	1/1	509.73/4.78	211.58/1.75	<0.0001*/0.2157
pH_i (−, *C*)	3.24/29.54	1/1	3.24/29.54	1.35/10.79	0.2728/0.0082*
AB	7.26/13.06	1/1	7.26/13.06	3.01/4.77	0.1133/0.0539
AC	59.84/101.39	1/1	59.84/101.39	24.84/37.05	0.0006*/0.0001*
BC	14.31/67.86	1/1	14.31/67.87	5.94/24.80	0.0350*/0.0006*
A^2	1206.73/4199.16	1/1	1206.73/4199.15	500.89/1534.41	<0.0001*/<0.0001*
B^2	154.09/1237.94	1/1	154.09/1237.94	63.96/452.35	<0.0001*/<0.0001*
C^2	1561.81/1273.64	1/1	1561.81/1273.64	648.28/465.40	<0.0001*/<0.0001*
Residual	24.09/27.37	10/10	2.41/2.74		
lack of fit	24.09/27.37	5/5	4.82/5.47		
pure error	0.00/0.00	5/5	0.00/0.00		
cor. Total	7026.03/6598.81	19/19			
std. dev.	1.55/1.65			R^2	0.9965/0.9958
Mean	40.38/33.63			adj. R^2	0.9935/0.9921
C.V. %	3.84/4.92			pred. R^2	0.9736/0.9679
PRESS	185.51/211.52			adeq. precision	49.7296/48.3519

[a]df degrees of freedom and * significant.

Experimental Design and Model Development. ACs of NRCBD for removal of SF and BCB were influenced individually or simultaneously by several parameters, such as concentration of SF/BCB (mg L^{-1}, *A*), temperature (°C, *B*), and pH_i (−, *C*). Therefore, optimization of parameters is essential to attain the highest ACs of NRCBD. However, measurement of individual and/or simultaneous effect(s) via one factor at a time is unempirical. Therefore, design of experiment has been introduced to reduce the number of experiments and measure the individual and/or simultaneous effect(s) through central composite design (CCD) analysis.

CCD Optimization of the Significant Variables. The CCD was introduced to understand the significant effects of individual and interactive effects of *A*, *B*, and C on ACs. The calculated ACs were interlinked with input variables for optimization using following empirical second-order polynomial equation (eq 2)

$$Y = \beta_0 + \sum_{m=1}^{3} \beta_m X_m + \sum_{m=1}^{3} \beta_{mm} {X_m}^2 + \sum_{m=1}^{3} \sum_{n=1}^{2} \beta_{mn} X_m X_n \quad (2)$$

Here, *Y*, β_0, and β_m, β_{mm}, and β_{mn} represent the predicted response, constant, and linear-, quadratic-, and interaction-coefficient, respectively. The CCD was executed involving 20 runs (Table S4) for each dye, in which *A*, *B*, and *C* were taken within 40.00−10.00 mg L^{-1}, 30.00−50.00 °C, and 8.00−12.00/7.00−11.00, respectively. The applicability of the model was examined by analyzing the analysis of variance (ANOVA) (Table 2). The process variables and actual- and predicted-response were listed in Table S4. Additionally, CCD analysis determined reliability of the quadratic model as compared to linear-, 2FI-, quadratic-, and cubic-model because of higher R^2, that is, 0.9966 and 0.9959 for SF and BCB, respectively, and close vicinity between adj. and pred. R^2, that is, 0.9935/0.9736 and 0.9921/0.9679 for SF and BCB, respectively.

From ANOVA table, *A*, *B*, *AC*, *BC*, A^2, B^2, and C^2 and *A*, *C*, *AC*, *BC*, A^2, B^2, and C^2 for SF and BCB, respectively, were noted to be significant (Table 2). The final equations obtained from the model in terms of actual factors were expressed using eqs 3 and 4.

$$R_{AC(SF)} = -415.42 + 4.41A + 4.046B + 61.59C - 0.0064AB - 0.012AC - 0.067BC + 0.042A^2 - 0.033B^2 - 2.82C^2 \quad (3)$$

$$R_{AC(BCB)} = -437.63 + 5.81A + 8.99B + 51.79C - 0.0086AB - 0.12AC - 0.15BC - 0.079A^2 - 0.093B^2 - 2.348C^2 \quad (4)$$

The three dimensional response surface plots (Figure 6a−f) showed the interactive effects among *AB*, *AC*, and *BC*. Finally, in the numerical optimization section, *A*, *B*, and *C* were considered in range, whereas ACs were considered to be the maximum. *A*, *B*, and *C* were found to be 31.15/28.64, 45.24/39.92, and 9.94/8.99 for SF/BCB, respectively.

Adsorption Isotherm Study. Mutual interactions between adsorbate (i.e., BCB, SF, and Hg(II)) and adsorbent (i.e., NRCBD) during isothermal adsorption was understood from the ACs/q_e of adsorbents. The residual adsorbate concentration (C_e) at equilibrium was fitted with Langmuir, Freundlich, Brunauer−Emmett−Teller (BET), and Sips isotherms (eqs 5−8).

$$q_e = q_{max} \frac{k_L C_e}{1 + k_L C_e} \quad (5)$$

$$q_e = k_F {C_e}^{1/n} \quad (6)$$

$$q_e = q_{BET} \frac{k_1 C_e}{(1 - k_2 C_e)(1 - k_2 C_e + k_1 C_e)} \quad (7)$$

$$q_e = q_{max} \frac{(k_S C_e)^{\gamma}}{1 + (k_S C_e)^{\gamma}} \quad (8)$$

Here, k_L, k_F, k_1, k_2, and k_S are isotherm constants and q_{max}, *n*, b_T, q_{BET}, and γ are isotherm parameters. Moreover, adsorption isotherm studies confirmed the fractional distribution of

DOI: 10.1021/acsomega.8b02799
ACS Omega 2019, 4, 421−436

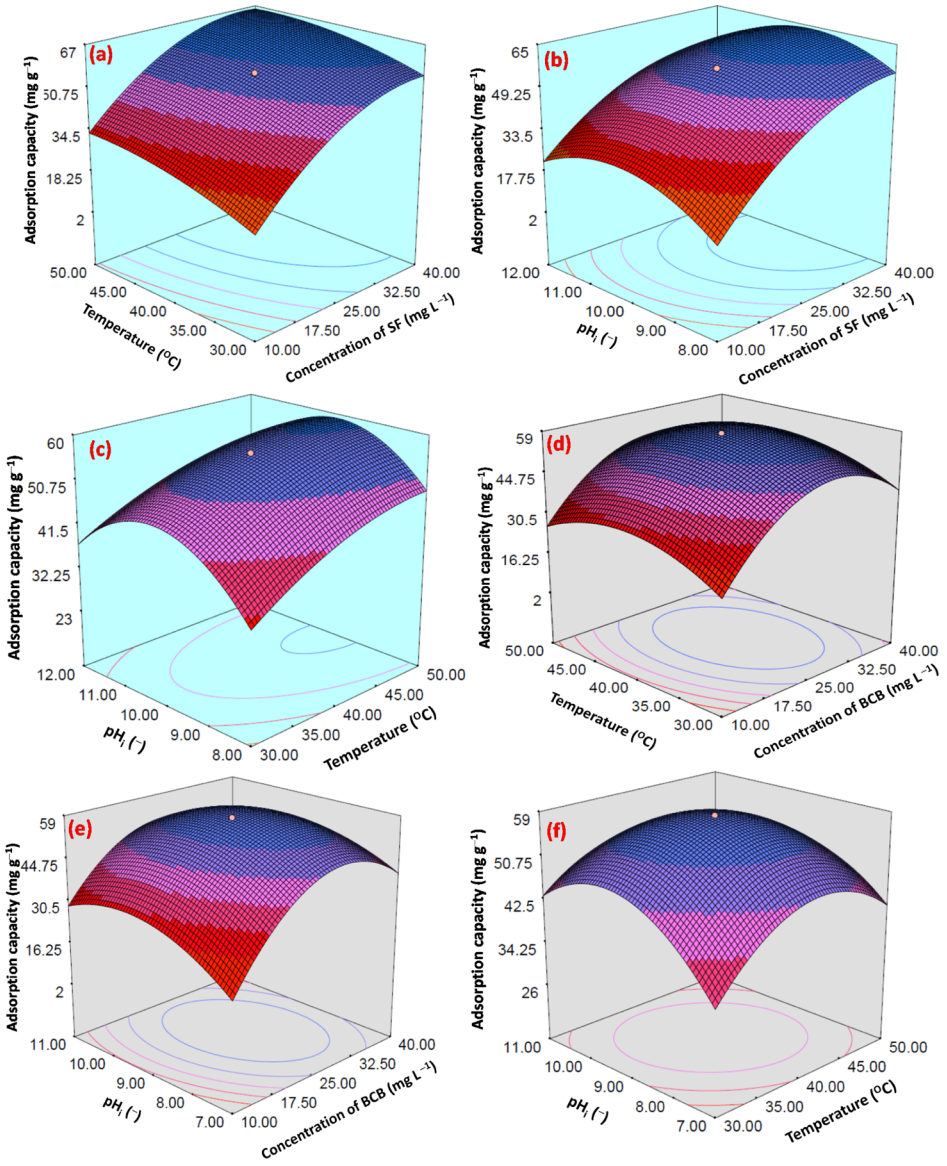

Figure 6. Three dimensional interactive RSM plots of AC vs (a) temperature (°C) and concentration of SF (mg L^{-1}), (b) pH_i (−) and concentration of SF (mg L^{-1}), and (c) pH_i (−) and temperature (°C) for SF and AC vs (d) temperature (°C) and concentration of BCB (mg L^{-1}), (e) pH_i (−) and concentration of BCB (mg L^{-1}), and (f) pH_i (−) and temperature (°C) for BCB.

adsorbate within solid and solution phases. In fact, the excellent performance potential of NRCBD was ascertained from high ACs and removal proficiency.

The adsorption isotherm studies were performed taking 0.01 g biocomposite and 50 mL buffer solutions within 5−40 ppm of dyes/Hg(II) at pH_i = 9.0/7.0 and 293−323 K. The Langmuir- and BET-model fitted the best for SF/Hg(II) and BCB, respectively, (Figure 7a−c), as evident from the highest R^2- and F-value (Table 3). Langmuir model predominantly considers the prevalence of monolayer adsorption onto the homogeneous surface of NRCBD. In this context, chemisorption of SF was understood from the temperature-dependent increase in k_L from 0.2172 to 0.3186. Indeed, the chemical interaction between $=N^+Me_2/=N^+HMe$ of SF and $-COO^-/-OH$ of NRCBD resulted in high q_{max}, which altered significantly from 280.17 to 348.36 mg g^{-1} with increase in temperature up to 323 K. The q_{max} of Hg(II) was relatively lower, that is, 166.46 mg g^{-1}, because of the strong ionic interaction-based adsorption and low concentrations. In this context, separation factor (R_L), a dimensionless quantity, measuring feasibility of any adsorption process, in which $R_L > 1$, $0 < R_L < 1$, $R_L = 1$ and $R_L = 0$ indicate unfavorable, favorable, linear, and irreversible adsorptions, respectively, was estimated using eq 9.

$$R_L = \frac{1}{1 + k_L C_0} \tag{9}$$

The spontaneity of adsorption was confirmed measuring R_L within 0.05−0.55 and 0.09−0.25 for SF and Hg(II), respectively.

Conversely, the preferential multilayer adsorption via dye−adsorbent and dye−dye interactions was ascertained from the best fitting of BCB adsorption data to the BET model. Moreover, an increase in q_{BET} and k_1 with increase in temperature from 293 to 323 K indicated more favorable adsorption at relatively higher temperatures. In fact, the reverse variation of k_2 with temperature indicated the decrease in dye−dye interactions at relatively higher temperatures because of the enhancement of average kinetic energy of dyes.

DOI: 10.1021/acsomega.8b02799
ACS Omega 2019, 4, 421−436

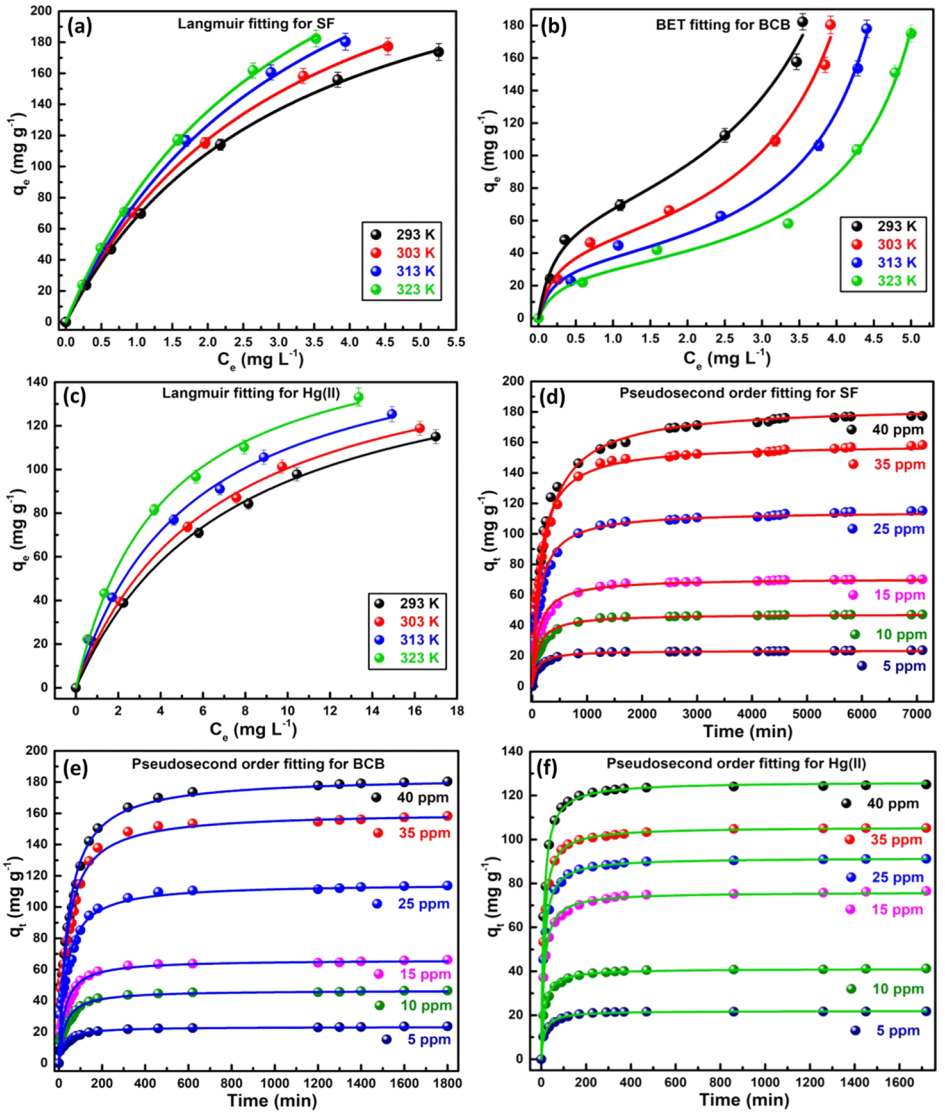

Figure 7. Langmuir fitting for (a) SF- and (c) Hg(II)-NRCBD and BET fitting for (b) BCB-NRCBD; pseudosecond order fitting for (d) SF-, (e) BCB-, and (f) Hg(II)-NRCBD.

Adsorption Kinetics Study. The mechanism of adsorption is identified by the rate determining step, mass transport, and diffusion processes. Herein, kinetics studies were carried out taking different initial concentrations of dyes/Hg(II), using 0.01 g of NRCBD at definite pH_i and four different temperatures (Figures 7d–f and S4a–c). Adsorption data of SF, BCB, and Hg(II) followed pseudosecond order kinetics at all temperatures because of the higher R^2-, F-value and the closest proximity between $q_{e,exp}$ and $q_{e,cal}$ (Table 3). All model fitted parameters support the chemisorption through ionic interaction between $-COO^-$ and O–H of NRCBD and SF/BCB/Hg(II), evidenced earlier in XPS (Figure 4) and FTIR analyses (Figure 3). Initially, a faster rate of chemisorption for SF, BCB, and Hg(II) was ascribed to the maximum population of functional groups onto the adsorbent surface, followed by the gradual decrease in rate, and finally, almost a constant rate at the equilibrium. The pseudosecond order rate constants (k_2) for SF and Hg(II) increased with the increase in temperature because of the elevated physicochemical interactions at higher temperatures. In spite of similar chemical structures, dye–dye and dye–NRCBD interactions resulted in the higher k_2 for BCB (Table 3). Thus, because of the molecular aggregation, $q_{e,exp}$ and $q_{e,cal}$ were greater for BCB as compared to SF within 293–303 K (Table 3), realised from TGA (Figure 5) and XRD (Figure S3). Thus, restricted the permeation of $(BCB)_2$ via tortuous path affected the rate of adsorption. However, larger overall molecular weight of $(BCB)_2$ than SF resulted in the higher amount of BCB onto the composite matrix (Table 3), and thus, q_e of BCB was higher than SF at 303 K.

$$q_t = q_e\left(1 - \frac{1}{1 - k_2 q_e t}\right) \tag{10}$$

$$q_t = q_e[1 - \exp(-k_1 t)] \tag{11}$$

Effect of Temperature on Adsorption Kinetics. The effect of temperature on chemisorption was envisaged taking 0.01 g NRCBD in 40 ppm solutions of both the dyes and Hg(II) at 293, 303, 313, and 323 K and pH_i = 9/7 (Figure S5a–c). Because both the dyes and Hg(II) followed pseudosecond order kinetics, activation energy of adsorption (E_a) was evaluated using the following Arrhenius type equation (eqs 12 and 13):

DOI: 10.1021/acsomega.8b02799
ACS Omega 2019, 4, 421–436

Table 3. Adsorption Isotherms and Kinetics Parameters

models parameters	temperature (K)			
	293	303	313	323
		Hg(II)		
		Langmuir		
q_{max} (mg g^{-1})/pH_i/C_0 (ppm)	164.07/7/5−40	166.46/7/5−40	168.69/7/5−40	170.38/7/5−40
k_L (L mg^{-1})	0.1361	0.1526	0.1853	0.2449
R^2/F	0.9978/4757.39	0.9976/4335.80	0.9969/3311.08	0.9978/4639.16
		Pseudosecond Order		
$q_{e,cal}$ (mg g^{-1})/pH_i/C_0 (ppm)	109.99/7/30	105.59/7/30	102.14/7/30	98.88/7/30
$q_{e,exp}$ (mg g^{-1})	110.26 ± 3.19	105.61 ± 3.27	101.32 ± 3.14	97.80 ± 3.03
k_2 (g mg^{-1} min^{-1})	6.34×10^{-4}	8.97×10^{-4}	11.20×10^{-4}	14.90×10^{-4}
R^2/F	0.9965/25 886.66	0.9993/135 522.05	0.9989/93 372.13	0.9983/64 517.33
		SF		
		Langmuir		
q_{max} (mg g^{-1})/pH_i/C_0 (ppm)	280.17/10/5−40	303.61/10/5−40	341.50/10/5−40	348.36/10/5−40
k_L (L mg^{-1})	0.2172	0.2652	0.2945	0.3186
R^2/F	0.9997/26 181.19	0.9996/21 697.13	0.9982/4781.31	0.9994/13 382.38
		Pseudosecond Order		
$q_{e,cal}$ (mg g^{-1})/pH_i/C_0 (ppm)	186.09/10/40	184.33/10/40	183.35/10/40	188.21/10/40
$q_{e,exp}$ (mg g^{-1})	173.72 ± 5.21	177.30 ± 5.32	180.30 ± 5.41	182.37 ± 5.47
k_2 (g mg^{-1} min^{-1})	1.63×10^{-5}	2.45×10^{-5}	3.26×10^{-5}	4.30×10^{-5}
R^2/F	0.9949/11 060.96	0.9906/6752.93	0.9928/10 330.26	0.9877/7193.79
		BCB		
		BET		
q_{BET} (mg g^{-1})/pH_i/C_0 (ppm)	64.66/9/5−40	46.14/9/5−40	35.22/9/5−40	30.10/9/5−40
k_1 (L mg^{-1})/k_2 (L mg^{-1})	4.6345/0.1795	4.7357/0.1879	5.0474/0.1816	3.7230/0.1664
R^2/F	0.9897/545.11	0.9906/588.00	0.9943/946.63	0.9930/752.02
		Pseudosecond Order		
$q_{e,cal}$ (mg g^{-1})/pH_i/C_0 (ppm)	190.10/9/40	183.41/9/30	175.69/9/30	169.69/9/30
$q_{e,exp}$ (mg g^{-1})	182.27 ± 5.47	180.40 ± 5.41	177.98 ± 5.34	174.99 ± 5.25
k_2 (g mg^{-1} min^{-1})	9.77×10^{-5}	1.31×10^{-4}	1.75×10^{-4}	2.30×10^{-4}
R^2/F	0.9891/4938.66	0.9854/4321.51	0.9740/2843.80	0.9737/3208.94

Table 4. Adsorption Thermodynamics Parameters for Hg(II)-/SF-/BCB-NRCBD

C_0 (ppm)	T (K)	$-\Delta G^0$ (kJ mol^{-1})	$-\Delta H^0$ (kJ mol^{-1})	$-\Delta S^0$ (J mol^{-1} K^{-1})
5	293	8.96/10.75/9.71	12.77/37.92/5.33	13.01/158.90/54.92
	303	8.84/11.33/10.31		
	313	8.66/11.86/11.36		
	323	8.59/12.40/12.29		
10	293	8.40/10.47/7.98	15.30/42.43/7.09	23.87/171.43/59.92
	303	7.97/11.06/9.40		
	313	7.71/11.66/10.94		
	323	7.71/12.27/13.21		
15	293	7.52/10.21/6.95	14.53/33.49/6.90	24.28/137.73/58.44
	303	7.03/10.81/8.17		
	313	6.90/11.42/9.45		
	323	6.77/11.95/11.14		
25	293	6.89/9.64/7.77	13.92/15.86/9.49	24.09/80.36/65.30
	303	6.55/10.26/8.41		
	313	6.40/11.01/9.20		
	323	6.15/11.57/10.20		
35	293	6.49/9.03/8.41	10.74/9.62/10.97	14.69/61.50/68.29
	303	6.20/9.71/9.02		
	313	6.15/10.45/9.63		
	323	6.02/11.05/10.25		
40	293	5.55/8.52/8.66	9.48/10.12/11.82	13.51/64.13/69.47
	303	5.34/9.23/9.32		
	313	5.22/9.95/9.96		
	323	5.15/10.60/10.58		

DOI: 10.1021/acsomega.8b02799
ACS Omega 2019, 4, 421−436

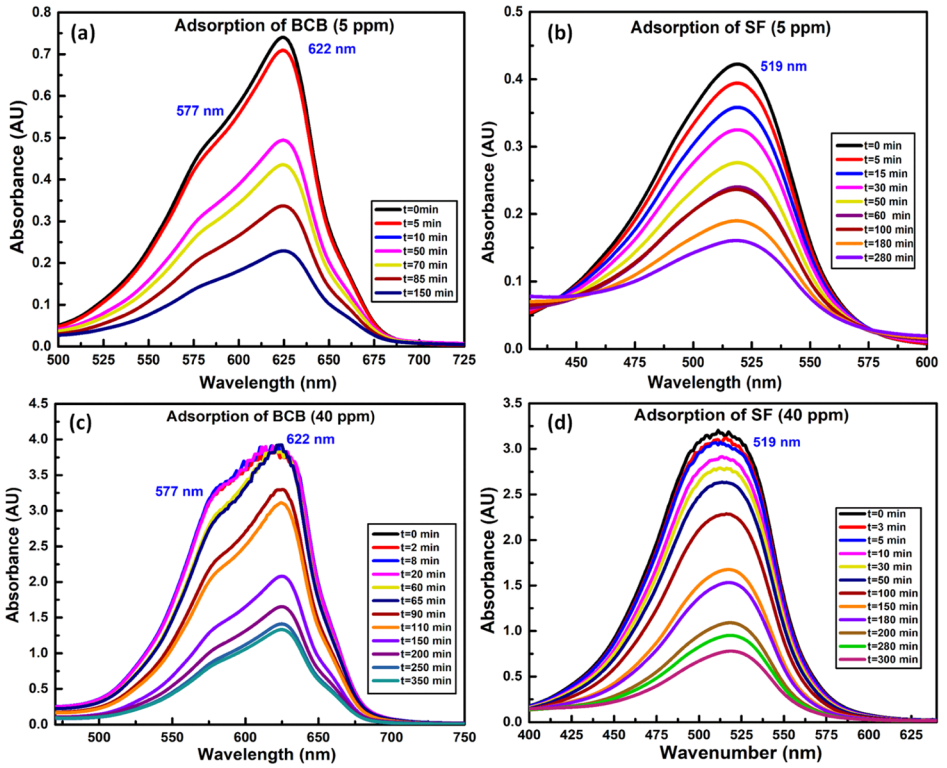

Figure 8. UV−vis spectrum of (a/c) BCB (5/40 ppm) and (b/d) SF (5/40 ppm).

$$k_2 = k_0 \exp(-E_a/RT) \tag{12}$$

that is

$$\ln k_2 = \ln k_0 - \frac{E_a}{RT} \tag{13}$$

Here, k_0, R, and T are temperature-independent factors (g mg^{-1} min^{-1}), universal gas constant (8.314 J mol^{-1} K^{-1}) and temperature (K), respectively. In fact, from the slope of ln k_2 vs $1/T$ plot, E_a of adsorption can be evaluated (Figure S5g). However, E_a values were: 25.26, 22.53, and 21.93 kJ mol^{-1} for SF, BCB, and Hg(II), respectively, inferred chemisorption for both the dyes/Hg(II).

Thermodynamics of Adsorption. The Gibbs free-energy change (ΔG^0) associated with the thermodynamic spontaneity of chemisorption was evaluated using eq 14.

$$\Delta G^0 = -RT \ln k_d \tag{14}$$

Here, k_d, that is, the distribution coefficient, is defined as the ratio of dye concentrations in solid to liquid phases at equilibrium (eq 15).

$$k_d = \frac{q_e}{C_e} \tag{15}$$

Here, q_e (mg g^{-1}) and C_e (mg L^{-1}) are equilibrium AC and residual concentration of adsorbate in the solution, respectively.

Thus, the slope and intercept of the linear plot of ln k_d vs $1/T$ (Figure S5d−f) of eq 16 determined ΔH^0 and ΔS^0, respectively (Table 2).

$$\ln k_d = -\frac{\Delta H^0}{RT} + \frac{\Delta S^0}{R} \tag{16}$$

Herein, the negative ΔG^0 for dyes and Hg(II) (Table 4) indicated spontaneous chemisorption.[46,47] However, gradual increase in $-\Delta G^0$ for adsorption of both the dyes and Hg(II) with the rise in temperature confirmed the enhancement of physicochemical interactions at relatively higher temperatures. In addition, the exothermic nature of adsorption was inferred from the negative ΔH^0 (Figure S5d−f), whereas positive ΔS^0 specified the increase in randomness at the solid−solution interface during adsorption of BCB, SF, and Hg(II).

UV−vis Studies on Adsorption of SF and BCB. The absorption spectra of concentrated aqueous solution of BCB envisaged an intense band at 622 nm and a shoulder at 577 nm because of the BCB-monomer and H-type dimer, respectively.[36] In this regard, the relative lowering in the intensity of the dimer-specific peak was ascribed to the increasing dilution with the progress of adsorption (Figure 8a,b). Indeed, such a dilution effect in minimizing the dimer population was also realized from the adsorption spectra of dilute aqueous solution of BCB showing significantly less prominent shoulder at 577 nm. On contrary, absorption spectra of SF were devoid of dimer-specific peaks because of lesser aggregating tendency of SF as compared to BCB (Figure 8c,d), presumed earlier from TGA analysis. Accordingly, because of the lack of dimers and lower aggregating tendency,[48] SF showed sterically favored faster adsorption onto NRCBD. In this regard, removal of SF and BCB were 76.01 and 64.5%, respectively, within 300 min, realized from the relatively faster time-dependent hypochromic change in the intensity of SF as compared to BCB (Figure 8). Moreover, deposition of ZnO and $Zn(OH)_2$ onto BCB-NRCBD, as determined from XPS and XRD results, hindered the adsorption of BCB onto NRCBD.

Desorption and Reusability. The recyclability of NRCBD was substantiated by studying adsorption at pH_i = 7.0 and 9.0/10.0 for Hg(II) and BCB/SF, respectively. Alongside, the desorption was carried out at pH_i = 2.0 and 0.1 M NaCl solution for Hg(II) and BCB/SF (Figure 9), respectively. In fact,

DOI: 10.1021/acsomega.8b02799
ACS Omega 2019, 4, 421−436

significantly higher adsorption up to 85% even after five adsorption−desorption cycles inferred excellent reusability of NRCBD.

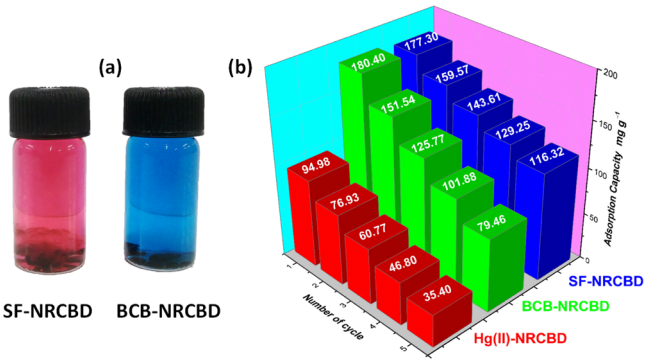

Figure 9. (a) Desorption of SF and BCB in 0.1 M NaCl solution; (b) reusability plots of Hg(II)-, BCB-, and SF-NRCBD.

Comparison of the Results. Different low cost natural, physically- and/or chemically-modified material(s), blends, homo-/co-/ter-polymers, and IPN-/composite-hydrogel have been employed for the adsorptive removal of Hg(II), BCB, and SF at varying temperatures (i.e., 288−323 K), pH_i, and initial concentrations (i.e., 1−3800 ppm) (Table S5). The ACs of NRCBD were excellent as compared to previously reported adsorbents.

CONCLUSIONS

The present work reports the nonsulfur curing of NR using Novolac components of waste CBD to fabricate collagenic material-based NRCBD−biocomposite superadsorbent showing very high removal proficiency and recyclability. The chromane mechanism of curing has been inferred from the arrival of chromane ring-specific peaks at 32.68, 74.01, 122.10, and 147.33 ppm in ^{13}C NMR and enormous lowering in peak intensities of olefinic carbons of NR, inferred from C 1s-/O 1s-XPS and FTIR analyses. Moreover, incorporation of nitrogen-based materials has been inferred from the appearance of MMU, 1,1-/1,3-DMU, and triazine ring-specific peaks in ^{13}C NMR, apprehended by FTIR and TGA analyses. The ionic interaction between $-COO^-$ and $=N^+Me_2/=N^+HMe$ of dyes/Hg(II) has been confirmed via extensive XPS and FTIR analyses. In comparison to SF, slightly delayed adsorption of BCB was attributed to the higher dimer forming ability of BCB as compared to SF because of the surface depositions of zinc oxide and zinc hydroxide, restricting the adsorption of BCB onto NRCBD, confirmed from XPS and XRD results, along with the measurements of isotherms, kinetics, and thermodynamics parameters. The collagenic-waste and NP-based NRCBD−biocomposite can be employed for fabricating CBD-cured other rubber adsorbents for decontamination and reuse of dyes and Hg(II). NRCBD showing excellent recyclability, performance characteristics, and outstanding adsorption efficiency has shown the novelty in a kinetically fast and thermodynamically spontaneous waste remediation process.

ASSOCIATED CONTENT

Supporting Information

The Supporting Information is available free of charge on the ACS Publications website at DOI: 10.1021/acsomega.8b02799.

Allyl hydrogen mechanism proposed by van der Meer; relative intensities of NR and NRCBD; FTIR analyses for NR, CBD, NRCBD, SF-, BCB-, and Hg(II)-NRCBD; XPS analyses for NRCBD, Hg(II)-, BCB-, and SF-NRCBD; design of experiment of CCD for SF/BCB; comparison table; DTG of NR, CBD, and NRCBD and NRCBD, Hg(II)-, SF-, and BCB-NRCBD; XRD of (a) SF and BCB, (b) NR, CBD, and NRCBD, and (d) NRCBD, BCB-, SF-, and Hg(II)-NRCBD; Field emission scanning electron microscopy photomicrographs of (a) NR, (b) CBD, (c) NRCBD, and (d) Hg(II)-NRCBD; (inset of d) energy-dispersive spectroscopy of Hg(II)-NRCBD; pseudosecond-order fitting of (a) SF-, (b) BCB-, and (c) Hg(II)-NRCBD; and Arrhenius-type fitting for (d) SF-, (e) BCB-, and (f) Hg(II)-NRCBD and (g) SF-/BCB-, Hg(II)-NRCBD (PDF)

AUTHOR INFORMATION

Corresponding Authors

*E-mail: drs.nrs@gmail.com (N.R.S.).
*E-mail: pkantichattopadhyay@gmail.com (P.K.C.).

ORCID

Nayan Ranjan Singha: 0000-0002-0219-1790

Notes

The authors declare no competing financial interest.

ACKNOWLEDGMENTS

The authors gratefully acknowledge the Department of Science and Technology (DST), Government of India (YSS/2015/000886), and the DST, Government of West Bengal (113(Sanc.)/ST/P/S&T/15G-2/2015), for providing financial assistance and the Department of Higher Education, Government of West Bengal for giving the opportunity to participate in inter institutional collaboration with the University of Calcutta. M.M. is grateful to the University Grants Commission, Government of India (sr. no. 2061410291, ref. no. 22/06/2014 (i) EU-V and roll no. 137632) for providing fellowship.

REFERENCES

(1) Hernández, M.; Grande, A. M.; Dierkes, W.; Bijleveld, J.; van der Zwaag, S.; García, S. J. Turning Vulcanized Natural Rubber into a Self-Healing Polymer: Effect of the Disulfide/Polysulfide Ratio. *ACS Sustainable Chem. Eng.* **2016**, *4*, 5776−5784.

(2) Lin, T.; Guo, B. Curing of Rubber via Oxa-Michael Reaction toward Significantly Increased Aging Resistance. *Ind. Eng. Chem. Res.* **2013**, *52*, 18123−18130.

(3) Lin, T.; Ma, S.; Lu, Y.; Guo, B. New Design of Shape Memory Polymers Based on Natural Rubber Crosslinked via Oxa-Michael Reaction. *ACS Appl. Mater. Interfaces* **2014**, *6*, 5695−5703.

(4) Ikeda, Y.; Yasuda, Y.; Hijikata, K.; Tosaka, M.; Kohjiya, S. Comparative Study on Strain-Induced Crystallization Behavior of Peroxide Cross-Linked and Sulfur Cross-Linked Natural Rubber. *Macromolecules* **2008**, *41*, 5876−5884.

(5) Klásek, A.; Vaněk, P. Vulcanization of Liquid Carboxyl-Terminated Rubber Filled with Leather Buffing Dust. *J. Appl. Polym. Sci.* **1994**, *53*, 735−746.

(6) Chronska, K.; Przepiorkowska, A. Buffing Dust as a Filler of Carboxylated Butadiene-Acrylonitrile Rubber and Butadiene-Acrylonitrile Rubber. *J. Hazard. Mater.* **2008**, *151*, 348−355.

(7) Senthil, R.; Hemalatha, T.; Manikandan, R.; Das, B. N.; Sastry, T. P. Leather Boards from Buffing Dust: A Novel Perspective. *Clean Technol. Environ. Policy* **2014**, *17*, 571−576.

(8) Gupta, V. K.; Suhas, I.; Ali, I.; Saini, V. K. Removal of Rhodamine B, Fast Green, and Methylene Blue from Wastewater using Red Mud,

DOI: 10.1021/acsomega.8b02799
ACS Omega 2019, 4, 421−436

an Aluminum Industry Waste. *Ind. Eng. Chem. Res.* **2004**, *43*, 1740−1747.
(9) Feng, X.; Li, P.; Qiu, G.; Wang, S.; Li, G.; Shang, L.; Meng, B.; Jiang, H.; Bai, W.; Li, Z.; Fu, X. Human Exposure To Methylmercury through Rice Intake in Mercury Mining Areas, Guizhou Province, China. *Environ. Sci. Technol.* **2008**, *42*, 326−332.
(10) Driscoll, C. T.; Mason, R. P.; Chan, H. M.; Jacob, D. J.; Pirrone, N. Mercury as a Global Pollutant: Sources, Pathways, and Effects. *Environ. Sci. Technol.* **2013**, *47*, 4967−4983.
(11) Zhou, Y.; Jin, Q.; Hu, X.; Zhang, Q.; Ma, T. Heavy Metal Ions and Organic Dyes Removal from Water by Cellulose Modified with Maleic Anhydride. *J. Mater. Sci.* **2012**, *47*, 5019−5029.
(12) Zhou, Y.; Hu, X.; Zhang, M.; Zhuo, X.; Niu, J. Preparation and Characterization of Modified Cellulose for Adsorption of Cd(II), Hg(II), and Acid Fuchsin from Aqueous Solutions. *Ind. Eng. Chem. Res.* **2013**, *52*, 876−884.
(13) Singha, N. R.; Karmakar, M.; Mahapatra, M.; Mondal, H.; Dutta, A.; Deb, M.; Mitra, M.; Roy, C.; Chattopadhyay, P. K. An *In Situ* Approach for the Synthesis of a Gum Ghatti-*g*-Interpenetrating Terpolymer Network Hydrogel for the High-Performance Adsorption Mechanism Evaluation of Cd(II), Pb(II), Bi(III) and Sb(III). *J. Mater. Chem. A* **2018**, *6*, 8078−8100.
(14) Singha, N. R.; Mahapatra, M.; Karmakar, M.; Dutta, A.; Mondal, H.; Chattopadhyay, P. K. Synthesis of Guar Gum-*g*-(Acrylic Acid-*co*-Acrylamide-*co*-3-Acrylamido Propanoic Acid) IPN via *In Situ* Attachment of Acrylamido Propanoic Acid for Analyzing Superadsorption Mechanism of Pb(II)/Cd(II)/Cu(II)/MB/MV. *Polym. Chem.* **2017**, *8*, 6750−6777.
(15) Singha, N. R.; Dutta, A.; Mahapatra, M.; Karmakar, M.; Mondal, H.; Chattopadhyay, P. K.; Maiti, D. K. Guar Gum-Grafted Terpolymer Hydrogels for Ligand-Selective Individual and Synergistic Adsorption: Effect of Comonomer Composition. *ACS Omega* **2018**, *3*, 472−494.
(16) Zhou, Y.; Wang, X.; Zhang, M.; Jin, Q.; Gao, B.; Ma, T. Removal of Pb(II) and Malachite Green from Aqueous Solution by Modified Cellulose. *Cellulose* **2014**, *21*, 2797−2809.
(17) Roy, S.; Singha, N. Polymeric Nanocomposite Membranes for Next Generation Pervaporation Process: Strategies, Challenges and Future Prospects. *Membranes* **2017**, *7*, 53.
(18) Singha, N. R.; Kar, S.; Ray, S. K. Synthesis of Novel Polymeric Membrane for Separation of MTBE-Methanol by Pervaporation. *Separ. Sci. Technol.* **2009**, *44*, 1970−1990.
(19) Singha, N. R.; Ray, S. K. Separation of Toluene-Methanol Mixtures by Pervaporation using Semi-IPN Polymer Membranes. *Separ. Sci. Technol.* **2010**, *45*, 2298−2307.
(20) Bergamasco, R.; Konradt-Moraes, L. C.; Vieira, M. F.; Fagundes-Klen, M. R.; Vieira, A. M. S. Performance of a Coagulation-Ultrafiltration Hybrid Process for Water Supply Treatment. *Chem. Eng. J.* **2011**, *166*, 483−489.
(21) Zhao, W.-Y.; Zhou, M.; Yan, B.; Sun, X.; Liu, Y.; Wang, Y.; Xu, T.; Zhang, Y. Waste Conversion and Resource Recovery from Wastewater by Ion Exchange Membranes: State-of-the-Art and Perspective. *Ind. Eng. Chem. Res.* **2018**, *57*, 6025−6039.
(22) Asnavandi, M.; Zhao, C. Hydrogen Bubble-Assisted Electrodeposition of Metal Nanoparticles from Protic Ionic Liquids for Electrocatalysis. *ACS Sustainable Chem. Eng.* **2016**, *5*, 85−89.
(23) Weber, C. C.; Wood, G. P. F.; Kunov-Kruse, A. J.; Nmagu, D. E.; Trout, B. L.; Myerson, A. S. Quantitative Solution Measurement for the Selection of Complexing Agents to Enable Purification by Impurity Complexation. *Cryst. Growth Des.* **2014**, *14*, 3649−3657.
(24) Zhou, Y.; Gao, B.; Zimmerman, A. R.; Chen, H.; Zhang, M.; Cao, X. Biochar-Supported Zerovalent Iron for Removal of Various Contaminants from Aqueous Solutions. *Bioresour. Technol.* **2014**, *152*, 538−542.
(25) Ikehata, K.; Zhao, Y.; Kulkarni, H. V.; Li, Y.; Snyder, S. A.; Ishida, K. P.; Anderson, M. A. Water Recovery from Advanced Water Purification Facility Reverse Osmosis Concentrate by Photobiological Treatment Followed by Secondary Reverse Osmosis. *Environ. Sci. Technol.* **2018**, *52*, 8588−8595.
(26) Gopalakannan, V.; Viswanathan, N. Development of Nano-Hydroxyapatite Embedded Gelatin Biocomposite for Effective Chromium(VI) Removal. *Ind. Eng. Chem. Res.* **2015**, *54*, 12561−12569.
(27) Mahapatra, M.; Karmakar, M.; Dutta, A.; Singha, N. R. Fabrication of Composite Membranes for Pervaporation of Tetrahydrofuran-Water: Optimization of Intrinsic Property by Response Surface Methodology and Studies on Vulcanization Mechanism by Density Functional Theory. *Korean J. Chem. Eng.* **2018**, *35*, 1889−1910.
(28) Karmakar, M.; Mahapatra, M.; Singha, N. R. Separation of Tetrahydrofuran Using RSM Optimized Accelerator-Sulfur-Filler of Rubber Membranes: Systematic Optimization and Comprehensive Mechanistic study. *Korean J. Chem. Eng.* **2017**, *34*, 1416−1434.
(29) Mahapatra, M.; Karmakar, M.; Dutta, A.; Mondal, H.; Roy, J. S. D.; Chattopadhyay, P. K.; Singha, N. R. Microstructural Analyses of Loaded and/or Unloaded Semisynthetic Porous Material for Understanding of Superadsorption and Optimization by Response Surface Methodology. *J. Environ. Chem. Eng.* **2018**, *6*, 289−310.
(30) Maeda, S.; Kunimoto, K.-K.; Sasaki, C.; Kuwae, A.; Hanai, K. Characterization of Microbial Poly(ε-L-lysine) by FT-IR, Raman and Solid State ^{13}C NMR Spectroscopies. *J. Mol. Struct.* **2003**, *655*, 149−155.
(31) Steinhof, O.; Kibrik, É. J.; Scherr, G.; Hasse, H. Quantitative and Qualitative ^{1}H, ^{13}C, and ^{15}N NMR Spectroscopic Investigation of the Urea-Formaldehyde Resin Synthesis. *Magn. Reson. Chem.* **2014**, *52*, 138−162.
(32) Wishart, D. S.; Bigam, C. G.; Holm, A.; Hodges, R. S.; Sykes, B. D. ^{1}H, ^{13}C and ^{15}N Random Coil NMR Chemical Shifts of the Common Amino Acids. I. Investigations of Nearest-Neighbor Effects. *J. Biomol. NMR* **1995**, *5*, 67−81.
(33) Matsuo, M.; Urano, S. ^{13}C NMR Spectra of Tocopherols and 2, 2-Dimethyl Chromanols. *Tetrahedron* **1976**, *32*, 229−231.
(34) Rolere, S.; Liengprayoon, S.; Vaysse, L.; Sainte-Beuve, J.; Bonfils, F. Investigating Natural Rubber Composition with Fourier Transform Infrared (FT-IR) Spectroscopy: A Rapid and Non-Destructive Method to Determine both Protein and Lipid Contents Simultaneously. *Polym. Test.* **2015**, *43*, 83−93.
(35) Lizarraga, E.; Gil, D. M.; Echeverría, G. A.; Piro, O. E.; Catalán, C. A. N.; Ben Altabef, A. Synthesis, Crystal Structure, Conformational and Vibrational Properties of 6-acetyl-2,2-dimethyl-chromane. *Spectrochim. Acta, Part A* **2014**, *127*, 74−84.
(36) Gilani, A. G.; Moghadam, M.; Hosseini, S. E.; Zakerhamidi, M. S. A Comparative Study on the Aggregate Formation of two Oxazine Dyes in Aqueous and Aqueous Urea Solutions. *Spectrochim. Acta, Part A* **2011**, *83*, 100−105.
(37) Singha, N. R.; Mahapatra, M.; Karmakar, M.; Mondal, H.; Dutta, A.; Deb, M.; Mitra, M.; Roy, C.; Chattopadhyay, P. K.; Maiti, D. K. In Situ Allocation of a Monomer in Pectin-*g*-Terpolymer Hydrogels and Effect of Comonomer Compositions on Superadsorption of Metal Ions/Dyes. *ACS Omega* **2018**, *3*, 4163−4180.
(38) Nicholas, N. J.; Franks, G. V.; Ducker, W. A. The Mechanism for Hydrothermal Growth of Zinc Oxide. *CrystEngComm* **2012**, *14*, 1232−1240.
(39) Karmakar, M.; Mahapatra, M.; Dutta, A.; Chattopadhyay, P. K.; Singha, N. R. Fabrication of Semisynthetic Collagenic Materials for Mere/Synergistic Adsorption: A Model Approach of Determining Dye Allocation by Systematic Characterization and Optimization. *Int. J. Biol. Macromol.* **2017**, *102*, 438−456.
(40) Takeyama, T.; Matsui, J. Recent Developments with Tire Cords and Cord-to-Rubber Bonding. *Rubber Chem. Technol.* **1969**, *42*, 159−256.
(41) Choudhury, S. D.; DasGupta, S.; Norris, G. E. Unravelling the Mechanism of the Interactions of Oxazolidine A and E with Collagens in Ovine Skin. *Int. J. Biol. Macromol.* **2007**, *40*, 351−361.
(42) Pourjavadi, A.; Kurdtabar, M. Collagen-Based Highly Porous Hydrogel without Any Porogen: Synthesis and Characteristics. *Eur. Polym. J.* **2007**, *43*, 877−889.
(43) Merline, D. J.; Vukusic, S.; Abdala, A. A. Melamine Formaldehyde: Curing Studies and Reaction Mechanism. *Polym. J.* **2012**, *45*, 413−419.

DOI: 10.1021/acsomega.8b02799
ACS Omega 2019, 4, 421−436

(44) Wu, B.; Mu, C.; Zhang, G.; Lin, W. Effects of Cr^{3+} on the Structure of Collagen Fiber. *Langmuir* **2009**, *25*, 11905−11910.
(45) Karmakar, M.; Mondal, H.; Mahapatra, M.; Chattopadhyay, P. K.; Chatterjee, S.; Singha, N. R. Pectin-grafted terpolymer superadsorbent via N-H activated strategic protrusion of monomer for removals of Cd(II), Hg(II), and Pb(II). *Carbohydr. Polym.* **2019**, *206*, 778−791.
(46) Chatterjee, S.; Gupta, A.; Mohanta, T.; Mitra, R.; Samanta, D.; Mandal, A. B.; Majumder, M.; Rawat, R.; Singha, N. R. Scalable Synthesis of Hide Substance-Chitosan-Hydroxyapatite: Novel Biocomposite from Industrial Wastes and Its Efficiency in Dye Removal. *ACS Omega* **2018**, *3*, 11486−11496.
(47) Mondal, H.; Karmakar, M.; Dutta, A.; Mahapatra, M.; Deb, M.; Mitra, M.; Roy, J. S. D.; Roy, C.; Chattopadhyay, P. K.; Singha, N. R. Tetrapolymer Network Hydrogels via Gum Ghatti-Grafted and N-H/C-H-Activated Allocation of Monomers for Composition-Dependent Superadsorption of Metal Ions. *ACS Omega* **2018**, *3*, 10692−10708.
(48) Sarkar, D.; Das, P.; Girigoswami, A.; Chattopadhyay, N. Spectroscopic Characterization of Phenazinium Dye Aggregates in Water and Acetonitrile Media: Effect of Methyl Substitution on the Aggregation Phenomenon. *J. Phys. Chem. A* **2008**, *112*, 9684−9691.

DOI: 10.1021/acsomega.8b02799
ACS Omega 2019, 4, 421−436